

WAVE BOTTOM BOUNDARY LAYER PHYSICS AND  
BED LOAD SEDIMENT TRANSPORT IN NEARSHORE

A Thesis

Presented in Partial Fulfillment of the Requirements for  
the Degree Master of Science in the  
Graduate School of The Ohio State University

By

Xiuying Xing, M.E.

\* \* \* \* \*

The Ohio State University

2004

Master's Examination Committee:

Dr. Diane L. Foster, Adviser

Dr. Thomas C. Lippmann

Dr. Michael R. Foster

Approved by

---

Adviser  
Civil Engineering Graduate  
Program

© Copyright by

Xiuying Xing

2004

## ABSTRACT

Energetics based bed load sediment transport models in which the quadratic stress law is assumed can accurately predict offshore sediment transport under current-dominated conditions. However, they cannot accurately predict onshore sediment transport under wave-dominated conditions. This study focuses on improving the modeling of beach scale bed load sediment transport due to waves over a flat bed. First, the small scale wave bottom boundary layer equation under arbitrary wave forcing is solved analytically with a zero-order eddy viscosity closure scheme. One of three temporally and/or spatially varying eddy viscosity assumptions is considered. The wave bottom boundary layer model is calibrated and evaluated by comparing the horizontal velocity and bed shear stress results with laboratory observations by Jonsson and Carlsen (1976) and Jensen *et al.* (1989), and field observations from the Duck94 field experiment (Foster *et al.*, 2000).

Predictions of bed stress from the three analytical boundary layer models are used for the formulations in three separate bed load flux models. The bed load flux models include an energetics based model and empirically based models of Meyer-Peter and Müller (1948) and Engelund and Fredsøe (1976). The three bed load models are evaluated with the discrete particle simulations of Drake and Calantoni (2001). Time-varying sediment flux predictions from all the three bed load models are comparable

to those from the discrete particle simulations of Drake and Calantoni (2001). Time-averaged sediment flux predictions show that the models predict onshore sediment flux under non-linear wave-dominated conditions, but the results are lower than the discrete particle simulations.

# WAVE BOTTOM BOUNDARY LAYER PHYSICS AND BED LOAD SEDIMENT TRANSPORT IN NEARSHORE

By

Xiuying Xing, M.S.

The Ohio State University, 2004

Dr. Diane L. Foster, Adviser

Energetics based bed load sediment transport models in which the quadratic stress law is assumed can accurately predict offshore sediment transport under current-dominated conditions. However, they cannot accurately predict onshore sediment transport under wave-dominated conditions. This study focuses on improving the modeling of beach scale bed load sediment transport due to waves over a flat bed. First, the small scale wave bottom boundary layer equation under arbitrary wave forcing is solved analytically with a zero-order eddy viscosity closure scheme. One of three temporally and/or spatially varying eddy viscosity assumptions is considered. The wave bottom boundary layer model is calibrated and evaluated by comparing the horizontal velocity and bed shear stress results with laboratory observations by Jonsson and Carlsen (1976) and Jensen *et al.* (1989), and field observations from the Duck94 field experiment (Foster *et al.*, 2000).

Predictions of bed stress from the three analytical boundary layer models are used for the formulations in three separate bed load flux models. The bed load flux models include an energetics based model and empirically based models of Meyer-Peter and Müller (1948) and Engelund and Fredsøe (1976). The three bed load models are evaluated with the discrete particle simulations of Drake and Calantoni (2001). Time-varying sediment flux predictions from all the three bed load models are comparable to those from the discrete particle simulations of Drake and Calantoni (2001). Time-averaged sediment flux predictions show that the models predict onshore sediment flux under non-linear wave-dominated conditions, but the results are lower than the discrete particle simulations.

## ACKNOWLEDGMENTS

I am very grateful to my adviser Dr. Diane Foster for giving me the great opportunity to work in this lab and giving me invaluable guidance and advise.

I am also grateful to Dr. Tom Lippmann and Dr. Michael Foster, my committee members, for helping me throughout my examination.

I would like to thank Doug Dusini and Heather Smith for answering my numerous questions in the research and thesis work. I would like to thank Parag Natoo and Allison Penko for the guidance on Dune2d. I would also like to thank Allison and Kim for helping me to revise my thesis.

I am so lucky to have been in such a nice work environment and would like to thank you again for your kindly help.

## VITA

March 1, 1976 ..... Born - Liaoning, China

1999 ..... B.E. Fluid Machinery and Fluid Engineering, Tsinghua University, China

2002 ..... M.E. Hydraulics and River Dynamics, Tsinghua University, China

2002-present ..... Graduate Research Associate, Ohio State University.

## FIELDS OF STUDY

Major Field: Civil Engineering

Studies in Coastal Engineering: Dr. Diane Foster

# TABLE OF CONTENTS

	Page
Abstract . . . . .	ii
Acknowledgments . . . . .	iv
Vita . . . . .	v
List of Tables . . . . .	viii
List of Figures . . . . .	ix
Chapters:	
1. Introduction . . . . .	1
1.1 Motivation . . . . .	1
1.2 Previous efforts . . . . .	2
1.3 Objectives and methods . . . . .	6
2. Wave bottom boundary layer model . . . . .	7
2.1 Wave bottom boundary layer governing equation . . . . .	7
2.2 Constant eddy viscosity . . . . .	10
2.3 Spatially varying eddy viscosity model . . . . .	16
2.4 Spatially and temporally varying eddy viscosity model . . . . .	20
3. Calibration and evaluation of the wave bottom boundary layer model . . . . .	23
3.1 Model calibration and evaluation with observations by Jonsson and Carlsen (1976) . . . . .	23
3.2 Model evaluation with observations by Jensen <i>et al.</i> (1989) . . . . .	31
3.3 Model evaluation with Duck94 field observations . . . . .	34

4.	Sediment transport model evaluations . . . . .	37
4.1	Simulated waveforms . . . . .	37
4.2	Time-varying sediment flux comparisons . . . . .	41
4.3	Time-averaged sediment flux comparisons . . . . .	49
5.	Conclusions . . . . .	56
Appendices:		
A.	Data analysis in Duck94 field experiment . . . . .	59
B.	Solution convergences of the bottom boundary layer models . . . . .	61

## LIST OF TABLES

Table	Page
3.1 Root-mean-square-deviations (msd) between the model predicted stresses and the measurements in the best-fit analysis. . . . .	24
3.2 Statistical comparisons of the predicted bed stresses of the bottom boundary layer models, Case 1, Case 2, and Case 3, and the BBB ( $c_f = 0.01$ ) models with laboratory observations by Jensen <i>et al.</i> (1989). $R^2$ , msd, and $\Delta\theta$ indicate the correlations, root-mean-square-deviations, and phase differences between the model predicted bed stresses and the measurements. . . . .	26
3.3 Statistical comparisons of the predicted peak velocities of Case 1, Case 2 and Case 3 with laboratory observations by Jonsson and Carlsen (1976). $R^2$ and msd indicate the correlations and the root-mean-square-deviations between the model predicted peak velocities and the observations. . . . .	26
3.4 Statistical comparisons of the predicted bed stresses by the bottom boundary layer models, Case 1, Case 2, and Case 3 with observations from the Duck94 field experiment. $\pm\Delta z$ means bed level measurement error is considered. $R^2$ and msd indicate the correlation coefficients and root-mean-square-deviations between the model predicted bed stresses and the Duck94 field observations. . . . .	35
4.1 Skewness and asymmetry of the waveforms. . . . .	39

## LIST OF FIGURES

Figure	Page
2.1 Bed shear stress contributions for the constant eddy viscosity (Case 1). The top panel presents the free stream velocity, the second panel presents the predicted bed stress (solid line), and the bed stress measured by Jonsson and Carlsen (1976) (dots). The third panel presents the first term of the predicted bed stress. The bottom panel presents the second term of the predicted bed stress for the 50 eigenvalues (solid line) and the first eigenvalue ( $\sigma = t$ ) condition (dashed line) solutions.	15
2.2 Bed shear stress contributions for spatially varying eddy viscosity (Case 2). The top panel presents the free stream velocity, the second panel presents the predicted bed stress (solid line), and the bed stress measured by Jonsson and Carlsen (1976) (dots). The bottom 3 panels present the first (second panel), second (third panel), and third (bottom panel) terms of the predicted bed stress for the 15 eigenvalues (solid line) and the first eigenvalue ( $\sigma = t$ ) condition (dashed line) solutions.	19
2.3 Bed shear stress contributions for the temporally and spatially varying eddy viscosity (Case 3). The top panel presents the free stream velocity, the second panel presents the predicted bed stress (solid line), and the bed stress measured by Jonsson and Carlsen (1976) (dots). The bottom 3 panels present the first (second panel), second (third panel), and third (bottom panel) terms of the predicted bed stress for the 15 eigenvalues (solid line) and the first eigenvalue ( $\sigma = t$ ) condition (dashed line) solutions.	22
3.1 Bed shear stress comparisons between the predicted values from Case 1 (dashed with dots), Case 2 (dashed), Case 3 (solid), and the quadratic stress law, and measured values by Jonsson and Carlsen (1976) (dots).	25

3.2 Comparisons between the predicted peak horizontal velocities of Case 1 (dashed with dots), Case 2 (dashed) and Case 3 (solid), and the observations by Jonsson and Carlsen (1976) (dots) at the peak velocity ( $\theta = 180^\circ$  in Figure 3.3). . . . . 27

3.3 Comparisons of the rms horizontal velocity ( $u_{rms}(\theta)$ ) calculated over the elevation at each wave phase for the Jonsson and Carlsen (1976) case. The top panel presents the free stream velocity, the bottom three panels present the bottom boundary layer models, Case 1, Case 2 and Case 3. ( $\cdot$ ) indicates the model results and ( $\times$ ) indicates observations by Jonsson and Carlsen (1976). Errorbars indicate  $\pm$  one root-mean-square-deviation ( $u_{msd}(\theta)$ ) between the model results and observations. 29

3.4 Comparisons of the rms horizontal velocity ( $u_{rms}(z)$ ) calculated over the wave phase at each elevation for Case 1, Case 2 and Case 3 (left to right panels, respectively) for the Jonsson and Carlsen (1976) case. ( $\cdot$ ) indicates the model results and ( $\times$ ) indicates observations by Jonsson and Carlsen (1976). Errorbars indicate  $\pm$  one root-mean-square-deviation ( $u_{msd}(z)$ ) between the model results and observations. The dashed lines indicate the bed level,  $z_o$ . . . . . 30

3.5 Comparisons of the rms horizontal velocity ( $u_{rms}(\theta)$ ) calculated over the elevation at each wave phase for the Jensen *et al.* (1989) case. The top panel presents the free stream velocity, the bottom three panels present the bottom boundary layer models, Case 1, Case 2, and Case 3. ( $\cdot$ ) indicates the model results and ( $\times$ ) indicates observations by Jensen *et al.* (1989). Errorbars indicate  $\pm$  one root-mean-square-deviation ( $u_{msd}(\theta)$ ) between the model results and observations. . . . . 32

3.6 Comparisons of the rms horizontal velocity ( $u_{rms}(z)$ ) calculated over the wave phase at each elevation for Case 1, Case 2 and Case 3 (left to right panels, respectively) for the Jensen *et al.* (1989) case. ( $\cdot$ ) indicates the model results and ( $\times$ ) indicates observations by Jensen *et al.* (1989). Errorbars indicate  $\pm$  one root-mean-square-deviation ( $u_{msd}(z)$ ) between the model results and observations. The dashed lines indicate the bed level,  $z_o$ . . . . . 33

3.7	A 30 sec time series of the free stream velocity (top) and the corresponding bed shear stresses comparisons (bottom) between the predictions from the bottom boundary layer models, Case 1 (dotted), Case 2 (dashed with dots), and Case 3 (dashed), and the field observations (solid). Shade area indicates the lower and upper boundary of the bed stress estimation when bed level measurement error is considered. Positive denotes onshore direction. . . . .	36
4.1	Waveforms for the sinusoidal (dotted), skewed ( $\phi = 0$ , solid line), combined ( $\phi = \pi/4$ , dashed line with dots), and asymmetric ( $\phi = \pi/2$ , dashed line) waves, with a 6 sec wave period and a 1.0 m/s maximum fluid velocity. Onshore directed flow is positive. . . . .	38
4.2	Comparisons of the rms of the bed shear stresses predicted by the bottom boundary layer models, Case 1 (squares), Case 2 (pluses), and Case 3 (diamonds) with the quadratic stress law ( $c_f = 0.01$ ) (x-coordinate) under sinusoidal, skewed ( $\phi = 0$ ), combined ( $\phi = \pi/4$ ), and asymmetric ( $\phi = \pi/2$ ) wave conditions. . . . .	40
4.3	Comparisons of the predicted time-varying sediment flux by energetics based (top panel), E-F (middle panel), and MP-M (bottom panel) bed load sediment transport models under a sinusoidal wave condition. . .	42
4.4	Comparisons of the predicted time-varying sediment flux by energetics based (top panel), E-F (middle panel), and MP-M (bottom panel) bed load sediment transport models under skewed wave condition ( $\phi = 0$ ). . . . .	44
4.5	Comparisons of the predicted time-varying sediment flux by energetics based (top panel), E-F (middle panel), and MP-M (bottom panel) bed load sediment transport models under combined wave condition ( $\phi = \pi/4$ ). . . . .	46
4.6	Comparisons of the predicted time-varying sediment flux by energetics based (top panel), E-F (middle panel), and MP-M (bottom panel) bed load sediment transport models under asymmetric wave condition ( $\phi = \pi/2$ ). . . . .	48

4.7	Comparisons of predicted time-averaged sediment flux by energetics based (top panel), E-F (middle panel), and MP-M (bottom panel) bed load sediment transport models with those simulated with the discrete particle model (Drake and Calantoni, 2001) under the skewed wave condition ( $\phi = 0$ ). The errorbars show the flux range with $\epsilon_b = 0.13 - 1.03$ . . . . .	53
4.8	Comparisons of the predicted time-averaged sediment flux by energetics based (top panel), E-F (middle panel), MP-M (bottom panel) bed load sediment transport models with those simulated with the discrete particle model (Drake and Calantoni, 2001) under the combined wave condition ( $\phi = \pi/4$ ). The errorbars show the flux range with $\epsilon_b = 0.13 - 1.03$ . . . . .	54
4.9	Comparisons of the predicted time-averaged sediment flux by energetics based (top panel), E-F(middle panel), and MP-M (bottom panel) bed load sediment transport models with those simulated with the discrete particle model (Drake and Calantoni, 2001) under the asymmetric wave condition ( $\phi = \pi/2$ ). The errorbars show the flux range with $\epsilon_b = 0.13 - 1.03$ . . . . .	55
B.1	The rms deviation between velocity results from the constant eddy viscosity model (Case 1) with a 50 cm upper boundary and with 10, 20, 30, and 40 cm upper boundaries normalized by the rms of the velocity results with a 50 cm upper boundary (left panel); the rms of the amplitude normalized by the rms of the first mode amplitude. . .	63
B.2	The rms deviation between velocity results from the spatially varying eddy viscosity model (Case 2) with a 50 cm upper boundary and with 10, 20, 30, and 40 cm upper boundaries normalized by the rms of the velocity results with a 50 cm upper boundary (left panel); the rms of the amplitude normalized by the rms of the first mode amplitude. . .	64
B.3	The rms deviation between velocity results from the temporally and spatially varying eddy viscosity model (Case 3) with a 50 cm upper boundary and with 10, 20, 30, and 40 cm upper boundaries normalized by the rms of the velocity results with a 50 cm upper boundary (left panel); the rms of the amplitude normalized by the rms of the first mode amplitude. . . . .	65

# CHAPTER 1

## INTRODUCTION

### 1.1 Motivation

Beach formation and evolution has a significant influence on the world's coastal population. The National Oceanic and Atmospheric Association estimates that half the population of the United States lives within 50 miles of a coast (Dalrymple, 2001). As the population pressure increases on the coasts, problems caused by beach erosion and sedimentation become more significant. Because of the societal impacts of beach erosion, there exists a need for the accurate prediction of sediment transport in coastal environments.

The study of sediment transport was first implemented by Einstein (1906), when he attempted to calculate the dispersion of solid grains due to fluid shear. Numerous theoretical sediment transport methods have since been proposed. With the significant increase of computing capabilities in last two decades, more sophisticated numerical models have been developed. The current approaches range from the resolution of individual grains to the resolution of the bottom boundary layer, and at the largest scale, the resolution of the entire beach.

Different sediment transport models often divide the transport into bed load and suspended load. Bed load, the movement of sediment close to the bed, is supposed to

be responsible for moving a major part of coarse grained sediment in the nearshore region. Suspended load is the transport of sediment through the water column due to influence of water-particle interactions and makes a smaller contribution to the bedform evolution when grains are coarse. Therefore, the investigation of bed load sediment transport is extremely important. Research has been done on this topic since the middle of 20th century (Meyer-Peter and Müller, 1948), but it is still not well understood.

## 1.2 Previous efforts

Granular scale models resolve the forces acting directly on individual grains. The computationally intensive simulations of Drake and Calantoni's (2001) discrete particle model is an example. The model solves Newton's second law ( $F = ma$ ) and a corresponding set of equations for the torques for each spherical grain to predict the movements of individual grains and the resulting total bed load transport. The model quantified the effect of fluid acceleration due to wave forms commonly observed in nature on the bed load transport. The authors found that pressure gradients generated by the surface gravity waves produce episodes of intense bed load transport, and the energetics based models can be modified to account for these effects by including a fluid acceleration term.

Boundary layer scale models resolve the bed load transport through the entire bed load layer. These models parameterize the motion of individual grains to resolve the temporal and spatial varieties of the bulk bed load layer. The earliest boundary-layer-scale bed load sediment transport model was introduced by Meyer-Peter and Müller (1948). The model is based on the assumption that grains will move when the

bed shear stress applied by flow,  $\tau_b$ , exceeds a critical value,  $\tau_c$ . The model assumes the non-dimensional bed load sediment transport,  $\phi_b$ , is proportional to the amount the non-dimensional bed stress exceeds the critical value,

$$\phi_b = 8(\theta - \theta_c)^{3/2} \quad (1.1)$$

where the non-dimensional bed stress is parameterized by the Shields parameter

$$\theta = \frac{\tau_b}{(S - 1)\rho g d_s} \quad (1.2)$$

where  $S$  is the specific gravity of sand,  $\rho$  is the density of flow,  $g$  is the acceleration due to gravity, and  $d_s$  is the sediment grain size.  $\theta_c$  is the critical Shield parameter.

The dimensional bed load,  $q_b$ , is defined with

$$q_b = \phi_b \sqrt{(S - 1)g d_s^3} \quad (1.3)$$

Similarly, Engelund and Fredsøe (1976) also developed a empirically based formula relating the non-dimensional sediment transport with the Shields parameter,

$$\phi_b = 5p(\sqrt{\theta} - 0.7\sqrt{\theta_c}) \quad (1.4)$$

with a probabilistic approach,  $p$ , to predict the fraction of grains moving in a bed load layer. Laboratory observations suggest (Fredsøe and Deigaard, 1992) that

$$p = [1 + (\frac{\pi}{6}\mu_d)^4]^{-1/4} \quad (1.5)$$

where  $\mu_d$  is the dynamic friction coefficient, and  $\phi$  is the angle of repose.

The dimensional bed load is

$$q_b = \phi_b \left[ \sqrt{(S - 1)g d_s^3} \left( \sqrt{\frac{2}{3} + \frac{36\nu^2}{(S - 1)g d_s^3}} - \sqrt{\frac{36\nu^2}{(S - 1)g d_s^3}} \right) \right] \quad (1.6)$$

where  $\nu$  is the flow viscosity. Both these formulations assume a known estimate of the bed stress.

Beach scale sediment transport models parameterize both the granular and boundary-layer-scale physics with empirical parameters to resolve the temporal and spatial evolution of shorelines and sand bars. These oscillatory flow models are based on the energetics principle of Bagnold (1966). Bagnold assumed the bed load transport is proportional to the work done by the flow,

$$q_b = K_b \tau_b u \quad (1.7)$$

where  $q_b$  is the local bed load sediment transport, and  $u$  is the horizontal velocity. For the flat bed case, the constant  $K_b$  is defined with

$$K_b = \frac{\rho_s}{g(\rho_s - \rho)} \frac{\epsilon_b}{\tan\phi} \quad (1.8)$$

where  $\rho_s$  and  $\rho$  are the densities of sediment and flow,  $\epsilon_b$  is the bed load efficiency, and  $\phi$  is the angle of repose.

Bailard (1981) and Bowen (1980) parameterized the bed stress with a quadratic stress law

$$\tau_b = \rho c_f u |u| \quad (1.9)$$

where  $c_f$  is the drag coefficient. They extended this principle for nearshore conditions to include both mean and oscillatory contributions (herein called the BBB model),

$$q_b = \frac{\rho_s}{g(\rho_s - \rho)} \rho c_f \frac{\epsilon_b}{\tan\phi} (|u|^2 \tilde{u} + |u|^2 \bar{u} - \frac{\tan\beta}{\tan\phi} |u|^3) \quad (1.10)$$

where  $\beta$  is the bed slope,  $u$  is the time-varying cross shore velocity that contains both mean,  $\bar{u}$ , and oscillatory,  $\tilde{u}$ , components.

Model-data comparisons by Thornton *et al.* (1996) and Gallagher *et al.* (1998) have shown that the BBB model is able to accurately predict the offshore migration of sandbars during high energy current-dominated conditions. However, it is unable to accurately predict onshore migration during moderate energy wave-dominated conditions. Recently Hsu *et al.* (2004) found that the model performance is improved when only the oscillatory velocity is included in the quadratic stress law. In this case, the energetics-based bed load sediment transport is given with

$$q_b = \rho_s \frac{c_f}{(S-1)g \tan\phi} \frac{\epsilon_b}{|\tilde{u}^2|} u \quad (1.11)$$

They found that the wave-averaged parameterization leads to increased skill in energetics model predictions of onshore sandbar migration.

In addition to the free stream velocity, acceleration has been recently considered to contribute to beach scale sediment transport models (Hsu and Hanes, 2004; Hoefel and Elgar, 2003; Elgar *et al.*, 2001). The prediction capability of energetics based bed load models have been improved with the inclusion of an empirically based fluid acceleration parameter (Drake and Calantoni, 2001; Hoefel and Elgar, 2003) (herein called the modified BBB model),

$$q_b = \begin{cases} k \langle u^3 \rangle + k_a (a_{spike} - a_{crit}) & a_{spike} \geq a_{crit} \\ k \langle u^3 \rangle & a_{spike} < a_{crit} \end{cases} \quad (1.12)$$

where  $k_a$  is an empirical constant and the acceleration parameter is

$$a_{spike} = \langle a^3 \rangle / \langle a^2 \rangle \quad (1.13)$$

where,  $\langle \rangle$  means time-averaged.

There are two possible explanations for the success of the empirical fluid acceleration parameter. First, the additional term may compensate for wave bottom boundary

layer physics not included in the quadratic stress law. Second, the horizontal pressure gradient may also induce incipient motion and transport of sediment (Sleath, 1999; Hsu and Hanes, 2004). The purpose of this thesis is to further investigate the bed shear stress from small scale wave bottom boundary layer models, therefore improving the beach-scale energetics based bed load sediment transport model.

### 1.3 Objectives and methods

This research is focused on improving the modeling of the beach scale bed load sediment transport due to waves over flat non-cohesive sediment beds. Three bed load sediment transport models, an energetics based model and the empirical bed load models of Meyer-Peter and Müller (1948) and Engelund and Fredsøe (1976), are developed with the inclusion of wave bottom boundary layer physics.

The small scale wave bottom boundary layer model is first established. The one-dimensional wave bottom boundary layer equations are analytically solved with one of three zero-order eddy viscosity schemes. The wave bottom boundary layer model is calibrated and evaluated by comparing the horizontal velocity and bed shear stress results with the laboratory observations by Jonsson and Carlsen (1976) and Jensen *et al.* (1989) and the field observations by Foster *et al.* (2000). The three bed load sediment transport models are evaluated with the discrete particle simulations of Drake and Calantoni (2001).

## CHAPTER 2

### WAVE BOTTOM BOUNDARY LAYER MODEL

#### 2.1 Wave bottom boundary layer governing equation

The fixed bed wave bottom boundary layer physics are approximated with the quasi-steady linearized wave bottom boundary layer equation (Nielsen, 1992)

$$\frac{\partial \hat{u}}{\partial t} + \frac{1}{\rho} \frac{dp}{dx} = \frac{1}{\rho} \frac{\partial \tau_{zx}}{\partial z} \quad (2.1)$$

where  $\hat{u}$  is the oscillatory velocity,  $p$  is the pressure, and  $\tau_{zx}$  is the shear stress. For linear free surface gravity waves, the pressure gradient is approximated with

$$\frac{1}{\rho} \frac{dp}{dx} = -\frac{du_{\infty}}{dt} \quad (2.2)$$

The shear stress,  $\tau_{zx}$ , is parameterized with

$$\tau_{zx} = \rho \nu_t \frac{\partial \hat{u}}{\partial z} \quad (2.3)$$

where  $\rho$  is the water density,  $\nu_t$  is the eddy viscosity. The boundary conditions are defined as

$$\begin{aligned} \hat{u}(d, t) &= u_{\infty} \\ \hat{u}(z_o, t) &= 0 \end{aligned} \quad (2.4)$$

and the initial condition is

$$\hat{u}(z, t_o) = \hat{r}_o(z) \quad (2.5)$$

where  $d$  is the upper boundary of the domain and is greater than the boundary layer thickness,  $\delta$ ,  $t_o$  is the initial time, and  $\hat{r}_o$  is an assumed initial velocity profile.  $z_o$  is the bed level, which following Nikuradse (1933) can be taken as

$$z_o = \frac{k_N}{30} \quad (2.6)$$

where  $k_N$  is the bed roughness. For a sand bottom, the grain roughness is assumed to be  $k_N = 2.5d_{50}$  (Fredsoe and Deigaard, 1992), where  $d_{50}$  is the grain size.

Here, we assume the eddy viscosity is a separable function in both time and space, and defined with

$$\nu_t = p(z)g(t) \quad (2.7)$$

The one-dimensional wave bottom boundary layer equation (2.1) can be analytically solved (Foster *et al.*, 1999). In order to eliminate the time-dependency of the free stream velocity at the upper boundary condition, a variable transformation is defined with

$$u = \hat{u} - \frac{z - z_o}{d - z_o} u_\infty \quad (2.8)$$

where  $u$  is the transformed cross shore boundary layer velocity. Inserting (2.8) into equation (2.1), the governing equation becomes

$$\frac{\partial u}{\partial t} - \frac{d - z}{d - z_o} \frac{\partial u_\infty}{\partial t} = \frac{\partial}{\partial z} \left( \nu_t \frac{\partial u}{\partial z} \right) + \frac{\partial \nu_t}{\partial z} \frac{u_\infty}{d - z_o} \quad (2.9)$$

with boundary conditions

$$\begin{aligned} u(d, t) &= 0 \\ u(z_o, t) &= 0 \end{aligned} \quad (2.10)$$

and initial condition

$$u(z, t_o) = r_o(z) = \hat{r}_o(z) - \frac{z - z_o}{d - z_o} u_\infty(t_o) \quad (2.11)$$

where  $r_o(z)$  is the transformed initial velocity profile.

To solve equation (2.9), the homogeneous terms are moved to the left side and forcing term to the right side as

$$\frac{\partial u}{\partial t} - g \frac{dp}{dz} \frac{\partial u}{\partial z} - pg \frac{\partial^2 u}{\partial z^2} = \frac{d - z}{d - z_o} \frac{\partial u_\infty}{\partial t} + g \frac{dp}{dz} \frac{u_\infty}{d - z_o} \quad (2.12)$$

The resulting homogeneous equation becomes

$$\frac{\partial u}{\partial t} - g \frac{dp}{dz} \frac{\partial u}{\partial z} - pg \frac{\partial^2 u}{\partial z^2} = 0 \quad (2.13)$$

with boundary conditions

$$\begin{aligned} u_p(d, t) &= 0 \\ u_p(z_o, t) &= 0 \end{aligned} \quad (2.14)$$

and initial condition

$$u_p(z, t_o) = r_o(z) \quad (2.15)$$

where  $u_p$  is the particular solution to the homogeneous equation. Using the separation of variables technique, let

$$u_p = \Psi(z)T(t) \quad (2.16)$$

and substitute into equation (2.13), resulting in

$$\frac{\dot{T}}{gT} = \frac{p\Psi'' + p'\Psi'}{\Psi} = -\lambda^2 \quad (2.17)$$

where  $(\dot{\phantom{x}})$  describes the derivative with respect to time  $t$ ,  $(\phantom{x})'$  represents the derivative with respect to  $z$ , and  $\lambda$  is a constant. Equation (2.17) is represented by two ordinary

differential equations containing  $t$  and  $z$  separately:

$$\dot{T} + \lambda^2 g T = 0 \quad (2.18)$$

and

$$p\Psi'' + p'\Psi' + \lambda^2\Psi = 0 \quad (2.19)$$

The solution for equation (2.18) is

$$T(t) = Ae^{(-\lambda^2 \int_0^t g(\tau)d\tau)} \quad (2.20)$$

where  $A$  is an integration constant. Solution for equation (2.19) is dependent on the assumption of  $p(z)$ .

In the following sections the velocity profile and bed shear stress are derived for each of three temporally and/or spatially varying eddy viscosities.

## 2.2 Constant eddy viscosity

In this case, the eddy viscosity is assumed to be constant in both time and space domains (herein Case 1) giving

$$\begin{aligned} \nu_t &= \kappa R_1 u_{*max} \\ p &= R_1 \\ g &= \kappa u_{*max} \end{aligned} \quad (2.21)$$

where  $\kappa$  is Von karman's constant,  $R_1$  is a constant,  $u_{*max}$  is the maximum bottom shear velocity, which is formulated by

$$u_{*max} = \sqrt{\frac{\tau_{max}}{\rho}} \quad (2.22)$$

and the maximum bed stress,  $\tau_{max}$ , is defined by Fredsøe and Deigaard (1992) as

$$\tau_{max} = \frac{1}{2}\rho f_w U_o^2 \quad (2.23)$$

where  $U_o$  is the amplitude of free stream velocity, and the friction factor,  $f_w$ , is defined as

$$f_w = 0.04 \left( \frac{A}{k_N} \right)^{-1/4} \quad (2.24)$$

when  $\frac{A}{k_N} > 50$ , which is satisfied in all cases in this thesis. Where

$$\begin{aligned} k_N &= 2.5d_{50} \\ A &= \frac{U_o T}{2\pi} \end{aligned}$$

in which  $d_{50}$  represents the grain size,  $T$  is the wave period, and  $U_o$  is the amplitude of the wave.

In this case, the solution for (2.18) becomes

$$T(t) = A e^{(-\lambda^2 \int_0^t g(\tau) d\tau)} = A e^{(-\lambda^2 R_1 \kappa u_{*max} t)} \quad (2.25)$$

With the assumption of  $p = R_1$ , equation (2.19) becomes

$$R_1 \Psi'' + \lambda^2 \Psi = 0 \quad (2.26)$$

The unique solution for (2.26) is

$$\Phi(y) = A_1 \cos\left(\sqrt{\frac{\lambda^2}{R_1}} y\right) + A_2 \sin\left(\sqrt{\frac{\lambda^2}{R_1}} y\right) \quad (2.27)$$

where  $y = z - z_o$ , with boundary conditions

$$\begin{aligned} \Psi(0) &= 0 \\ \Psi(d - z_o) &= 0 \end{aligned} \quad (2.28)$$

The unique solution to satisfy the boundary conditions (2.28) is

$$\Psi(z) = \sin\left(\sqrt{\frac{\lambda^2}{R_1}}(z - z_o)\right) \quad (2.29)$$

The complete homogeneous solution for (2.13) becomes

$$u_p(z, t) = \sum_{n=1}^{\infty} b_n \sin\left(\sqrt{\frac{\lambda^2}{R_1}}(z - z_o)\right) e^{(-\lambda^2 R_1 \kappa u_{*max} t)} \quad (2.30)$$

where the new integration constant,  $b_n$ , is

$$b_n = \frac{1}{c_n} \int_{z_o}^d r_o(z) \Psi(z) dz \quad (2.31)$$

and the constant  $c_n$  satisfies the orthogonality condition,

$$\int_{z_o}^d \Psi_n(z) \Psi_m(z) dz = \begin{cases} 0 & \text{if } m \neq n \\ c_n & \text{if } m = n \end{cases} \quad (2.32)$$

The homogeneous solution is obtained by rearranging the non-homogeneous equation (2.9) to

$$\frac{\partial u}{\partial t} = \frac{\partial}{\partial z} \left( \nu_t \frac{\partial u}{\partial z} \right) + F(z, t) \quad (2.33)$$

where the forcing term,  $F(z, t)$ , is the right-hand side of (2.12) as a function of the free stream acceleration

$$F(z, t) = \frac{d - z}{d - z_o} \frac{du_{\infty}}{dt} \quad (2.34)$$

Equation (2.33) is solved by assuming a series solution for the velocity of the form

$$u(z, t) = \sum_{n=1}^{\infty} a_n(t) \Psi_n(z) \quad (2.35)$$

where  $\Psi_n(z)$  is known from (2.27), and  $a_n(t)$  is determined by substituting (2.35) into (2.33),

$$\sum_{n=1}^{\infty} \dot{a}_n \Psi_n = gp \sum_{n=1}^{\infty} a_n \Psi_n'' + F \quad (2.36)$$

Furthermore, assuming  $F$  can also be represented with a series solution as

$$F(z, t) = \sum_{n=1}^{\infty} F_n(t) \Psi_n(z) \quad (2.37)$$

and  $F_n$  is determined with

$$F_n(t) = \frac{1}{c_n} \int_{z_o}^d F(z, t) \Psi_n(z) dz \quad (2.38)$$

Substituting (2.37) into (2.36),  $\Psi_n$  can be eliminated, then (2.36) is simplified to

$$\dot{a}_n(t) + \lambda_n^2 g a_n(t) = F_n(t) \quad (2.39)$$

Multiplying both sides of (2.39) by  $e^{(\lambda_n^2 \int_0^t g(\tau) d\tau)}$  and combining the left-hand side into one derivative with respect to time

$$\frac{d}{dt} [e^{(\lambda_n^2 \int_0^t g(\tau) d\tau)} a_n(t)] = F_n(t) e^{(\lambda_n^2 \int_0^t g(\tau) d\tau)} \quad (2.40)$$

Integrating (2.40) with respect to time results in an expression for the amplitude function

$$a_n(t) = a_n(0) e^{(-\lambda_n^2 \int_0^t g(\tau) d\tau)} + \int_0^t F_n(\sigma) e^{(-\lambda_n^2 \int_\sigma^t g(\tau) d\tau)} d\sigma \quad (2.41)$$

with the initial condition,  $a_n(0) = b_n$ . The first term in (2.41) is the transient component which depends on the initial condition and decays quickly to zero after the initial time,  $t_o$ . The complete solution to (2.1) is

$$\hat{u}(z, t) = \sum_{n=1}^{\infty} a_n(t) \Psi_n(z) + \frac{z - z_o}{d - z_o} u_\infty \quad (2.42)$$

where

$$\Psi_n(z) = \sin\left(\sqrt{\frac{\lambda_n^2}{R_1}} (z - z_o)\right) \quad (2.43)$$

In this case,  $g$  is a constant, thus  $\int_0^t g(\tau) d\tau = gt$ , and  $\int_\sigma^t g(\tau) d\tau = g(t - \sigma)$  in equation (2.40) and (2.41).

Substituting the velocity solution (2.42) into shear stress formulation (2.3), the bed shear stress becomes

$$\begin{aligned} \tau_{zx}|_{z=z_o} = & \rho\kappa R_1 u_{*max} \left\{ \frac{u_\infty}{d - z_o} \right. \\ & \left. + \sum_{n=1}^{\infty} \frac{-\lambda_n z_o^{-\frac{1}{2}} E_n K_n}{c_n} \int_0^t \frac{du_\infty}{d\sigma} e^{-\lambda_n^2 (t-\sigma)\kappa R_1 u_{*max}} d\sigma \right\} \end{aligned} \quad (2.44)$$

where

$$\begin{aligned} K_n &= \int_{z_o}^d \frac{d-z}{d-z_o} \sin\left(\sqrt{\frac{\lambda_n^2}{R_1}}(z-z_o)\right) dz \\ E_n &= \sqrt{\frac{\lambda_n^2}{R_1}} \end{aligned}$$

where  $K_n$  and  $E_n$  are constants, and are a function of the eigenvalues,  $\lambda_n$ .

There are two terms in the shear stress formula (2.44). The first term has the form of a quadratic stress law, which is negligible compared with the second term (about 1/10) when  $d \gg z_o$  (Figure 2.1). Considering only the first eigenvalue and  $\sigma = t$  condition, the integral in the second term goes to  $u_\infty$ , thus the temporal term will also have the form of quadratic stress law. However, when more eigenvalues are included and the convolution integral is completed, the formulation predicts a phase lag between the free stream velocity and the shear stress.

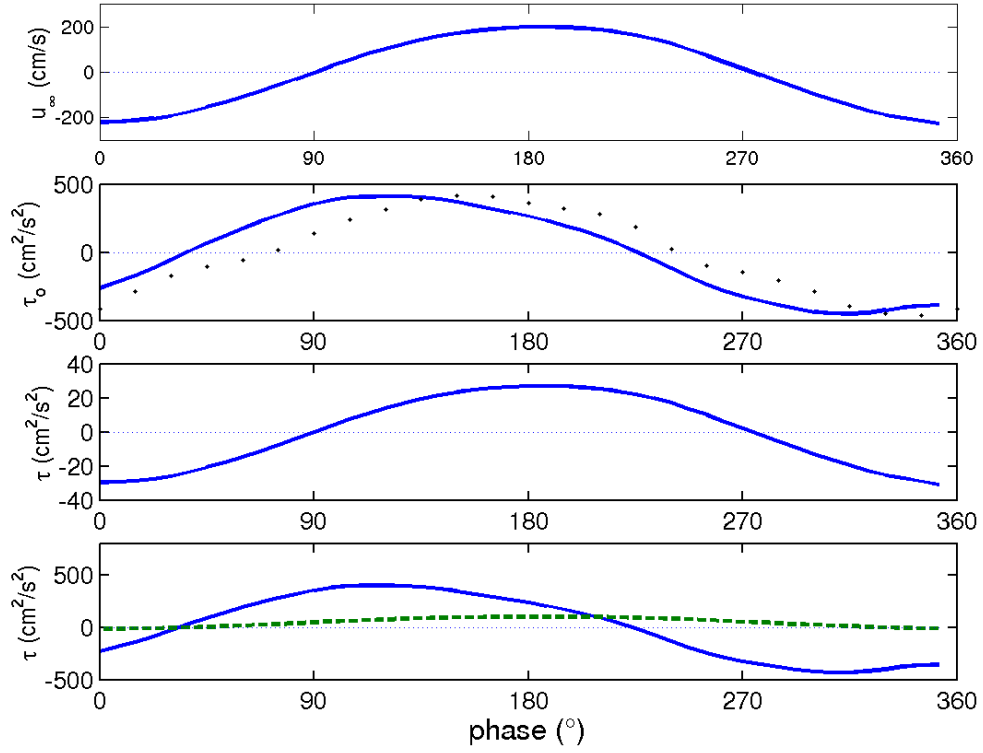


Figure 2.1: Bed shear stress contributions for the constant eddy viscosity (Case 1). The top panel presents the free stream velocity, the second panel presents the predicted bed stress (solid line), and the bed stress measured by Jonsson and Carlsen (1976) (dots). The third panel presents the first term of the predicted bed stress. The bottom panel presents the second term of the predicted bed stress for the 50 eigenvalues (solid line) and the first eigenvalue ( $\sigma = t$ ) condition (dashed line) solutions.

### 2.3 Spatially varying eddy viscosity model

In this case, the eddy viscosity is assumed to be constant in time and increases linearly in space (herein Case 2) giving

$$\begin{aligned}\nu_t &= R_2 \kappa z u_{*max} \\ p(z) &= z \\ g &= R_2 \kappa u_{*max}\end{aligned}\tag{2.45}$$

where  $R_2$  is a constant,  $z$  is the vertical coordinate, and  $\kappa$  and  $u_{*max}$  have the same meaning as in Case 1.

In this case, the solution for (2.18) becomes

$$T(t) = A e^{(-\lambda^2 \int_0^t g(\tau) d\tau)} = A e^{(-\lambda^2 R_2 \kappa u_{*max} t)}\tag{2.46}$$

With the assumption of  $p = z$ , equation (2.19) becomes

$$z\Psi'' + \Psi' + \lambda^2\Psi = 0\tag{2.47}$$

with the same boundary condition as in Case 1 given by (2.28).

The solution for (2.47) is a zeroth order Bessel functions of the first ( $J_o$ ) and the second kinds ( $Y_o$ )

$$\Psi(y) = B_1 J_o(2\lambda z^{\frac{1}{2}}) + B_2 Y_o(2\lambda z^{\frac{1}{2}})\tag{2.48}$$

where  $B_1$  and  $B_2$  are integration constants and are determined from the lower boundary condition. The upper boundary condition requires that the eigenvalues,  $\lambda_n$ , satisfy the eigenfunctions

$$J_o(2\lambda_n z_o^{\frac{1}{2}}) Y_o(2\lambda_n d^{\frac{1}{2}}) - Y_o(2\lambda_n z_o^{\frac{1}{2}}) J_o(2\lambda_n d^{\frac{1}{2}}) = 0\tag{2.49}$$

The complete homogeneous solution for (2.13) becomes

$$u_p(z, t) = \sum_{n=1}^{\infty} b_n (J_o(2\lambda_n z_o^{\frac{1}{2}}) Y_o(2\lambda_n z^{\frac{1}{2}}) - Y_o(2\lambda_n z_o^{\frac{1}{2}}) J_o(2\lambda_n z^{\frac{1}{2}})) e^{(-\lambda^2 R_2 \kappa u_{*max} t)} \quad (2.50)$$

where the integration constants,  $b_n$ , have the same form as in Case 1 given by (2.31), and the constants,  $c_n$ , also satisfy (2.32).

Rearranging the non-homogeneous equation (2.9) to (2.33), the time-varying forcing term,  $F(z, t)$ , is a function of the free stream acceleration and velocity

$$F(z, t) = \frac{d-z}{d-z_o} \frac{du_{\infty}}{dt} + g(t) \frac{u_{\infty}}{d-z_o} \quad (2.51)$$

As in Case 1 (2.35), assume a series solution for the velocity defined with

$$\sum_{n=1}^{\infty} \dot{a}_n \Psi_n = g \sum_{n=1}^{\infty} a_n (p\Psi_n)' + F(z, t) \quad (2.52)$$

where  $F(z, t)$  and  $F_n(t)$  are defined with (2.37) and (2.38). The resulting amplitude function has the form of (2.41) with an initial condition,  $a_n(0) = b_n$ . The first term in (2.41) is a transient component which depends on the initial condition and quickly decays to zero after the initial time,  $t_o$ . In this case, the complete solution to (2.1) has the same form as (2.42), but the eigenfunctions become

$$\Psi_n(z) = Y_o(2\lambda_n z_o^{\frac{1}{2}}) J_o(2\lambda_n z^{\frac{1}{2}}) - J_o(2\lambda_n z_o^{\frac{1}{2}}) Y_o(2\lambda_n z^{\frac{1}{2}}) \quad (2.53)$$

Here,  $g(t)$  is also a constant, thus  $\int_0^t g(\tau) d\tau = gt = R_2 \kappa u_{*max}$ , and  $\int_{\sigma}^t g(\tau) d\tau = g(t - \sigma) = R_2 \kappa u_{*max}(t - \sigma)$  in equation (2.40) and (2.41).

Substituting the velocity solution (2.42) into shear stress formulation (2.3), the bed shear stress becomes

$$\begin{aligned}
\tau_{zx}|_{z=z_o} &= \rho\kappa R_2 z_o u_{*max} \left\{ \frac{u_\infty}{d - z_o} \right. \\
&+ \sum_{n=1}^{\infty} \frac{-\lambda_n z_o^{-\frac{1}{2}} E_n K_{n1}}{c_n} \int_0^t \frac{du_\infty}{d\sigma} e^{-\lambda_n^2 (t-\sigma)\kappa R_2 u_{*max}} d\sigma \\
&+ \left. \sum_{n=1}^{\infty} \frac{-\lambda_n z_o^{-\frac{1}{2}} E_n K_{n2}}{c_n} \int_0^t u_\infty e^{-\lambda_n^2 (t-\sigma)\kappa R_2 u_{*max}} d\sigma \right\} \quad (2.54)
\end{aligned}$$

where

$$\begin{aligned}
K_{n1} &= \int_{z_o}^d \frac{d - z_o}{d - z} [Y_0(2\lambda_n z_o^{\frac{1}{2}}) J_0(2\lambda_n z^{\frac{1}{2}}) - J_0(2\lambda_n z_o^{\frac{1}{2}}) Y_0(2\lambda_n z^{\frac{1}{2}})] dz \\
K_{n2} &= \kappa R_2 u_{*max} \int_{z_o}^d \frac{1}{d - z_o} [Y_0(2\lambda_n z_o^{\frac{1}{2}}) J_0(2\lambda_n z^{\frac{1}{2}}) - J_0(2\lambda_n z_o^{\frac{1}{2}}) Y_0(2\lambda_n z^{\frac{1}{2}})] dz \\
E_n &= Y_0(2\lambda_n z_o^{\frac{1}{2}}) J_1(2\lambda_n z_o^{\frac{1}{2}}) - J_0(2\lambda_n z_o^{\frac{1}{2}}) Y_1(2\lambda_n z_o^{\frac{1}{2}})
\end{aligned}$$

$K_{n1}$ ,  $K_{n2}$ ,  $c_n$  and  $E_n$  are functions of eigenvalues,  $\lambda_n$ .

Figure 2.2 shows the relative contributions from each of the shear stress terms in (2.54). The first term in (2.54) has the form of a quadratic stress law, but contributes a negligible fraction (about 1/100) of the total stress when  $d \gg z_o$ . It has the same phase as the free stream velocity (see the third panel of Figure 2.2). As with Case 1, the second term reduces to a quadratic stress law when only the first eigenvalue is included and  $\sigma = t$  condition is considered. A similar assumption for the integral in the third term results in a contribution from the horizontal, which has a  $\pi/4$  phase difference with the free stream velocity and is in phase with the free stream accelerations (see the bottom panel of Figure 2.2). When more eigenvalues are included and the convolution integral is completed, the second term (velocity-related) in the shear stress predicts a phase lead while the third term (acceleration-related) predicts

a phase lag to the free stream velocity. The third term contributes about 1/5 of the total stress.

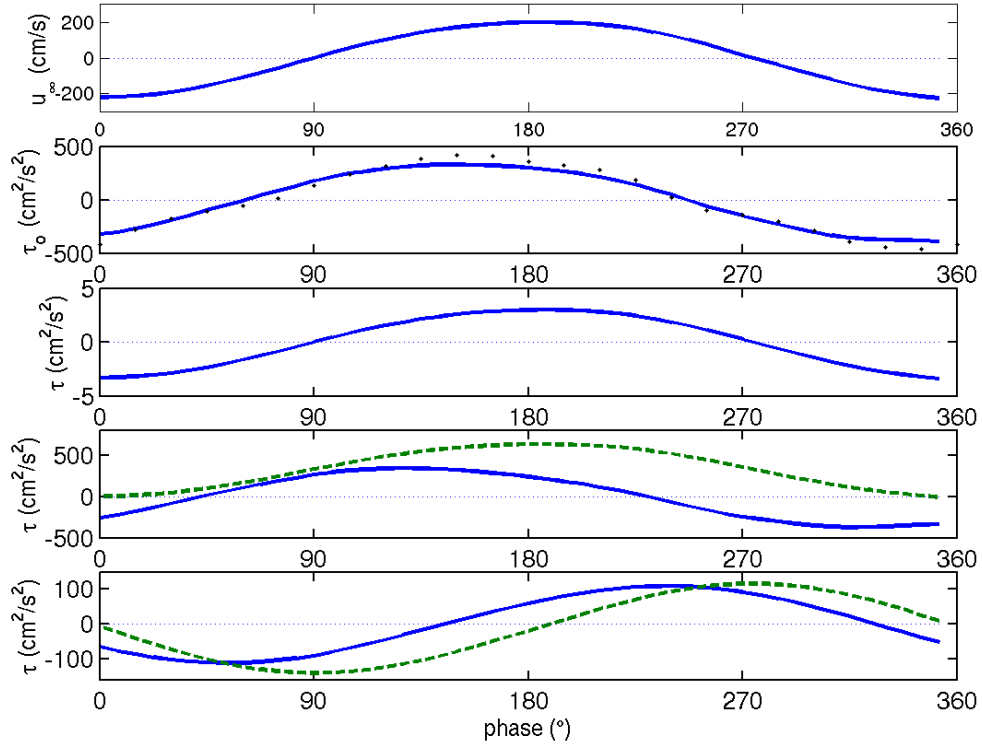


Figure 2.2: Bed shear stress contributions for spatially varying eddy viscosity (Case 2). The top panel presents the free stream velocity, the second panel presents the predicted bed stress (solid line), and the bed stress measured by Jonsson and Carlsen (1976) (dots). The bottom 3 panels present the first (second panel), second (third panel), and third (bottom panel) terms of the predicted bed stress for the 15 eigenvalues (solid line) and the first eigenvalue ( $\sigma = t$ ) condition (dashed line) solutions.

## 2.4 Spatially and temporally varying eddy viscosity model

For this case, the eddy viscosity is assumed to vary in time and increase linearly in space (herein called Case 3),

$$\begin{aligned} \nu_t &= \kappa z R_3 |u_\infty(t)| \\ p(z) &= z \\ g(t) &= \kappa R_3 |u_\infty(t)| \end{aligned} \tag{2.55}$$

where  $R_3$  is a constant and  $|u_\infty|$  is the amplitude of the free stream velocity.

In this case, the solution for (2.18) becomes

$$T(t) = A e^{(-\lambda^2 \int_0^t g(\tau) d\tau)} = A e^{(-\lambda^2 \int_0^t \kappa R_3 |u_\infty(\tau)| d\tau)} \tag{2.56}$$

With the assumption of  $p = z$ , equation (2.19) has the same form as (2.47) with the same boundary condition (2.28). The solution for (2.47) is also given by (2.48). The resulting total velocity has the form of (2.42), where the amplitude function,  $a_n(t)$ , is given by (2.41), and the eigenfunction,  $\Psi_n(z)$ , is given by (2.53).

Unlike Case 1 and 2,  $g(t)$  is not a constant. In this case, the integrals in the amplitude function (2.41) become

$$\begin{aligned} \int_0^t g(\tau) d\tau &= \kappa R_3 \int_0^t |u_\infty(\tau)| d\tau \\ \int_\sigma^t g(\tau) d\tau &= \kappa R_3 \int_\sigma^t |u_\infty(\tau)| d\tau \end{aligned} \tag{2.57}$$

Substituting the velocity solution (2.42) into shear stress formulation (2.3), the bed shear stress becomes

$$\begin{aligned}
\tau_{zx}|_{z=z_o} &= \rho\kappa R_3 z_o |u_\infty(t)| \left\{ \frac{u_\infty}{d-z_o} \right. \\
&+ \sum_{n=1}^{\infty} \frac{-\lambda_n z_o^{-\frac{1}{2}} E_n K_{n1}}{c_n} \int_0^t \frac{du_\infty}{d\sigma} e^{-\lambda_n^2 \kappa R_3 \int_\sigma^t |u_\infty| d\tau} d\sigma \\
&+ \left. \sum_{n=1}^{\infty} \frac{-\lambda_n z_o^{-\frac{1}{2}} E_n K_{n2}}{c_n} \int_0^t u_\infty |u_\infty| e^{-\lambda_n^2 \kappa R_3 \int_\sigma^t |u_\infty| d\tau} d\sigma \right\} \quad (2.58)
\end{aligned}$$

where  $K_{n1}$  and  $E_n$  have the same forms as in Case 2, but

$$K_{n2} = \kappa R_3 \int_{z_o}^d \frac{1}{d-z_o} [Y_0(2\lambda_n z_o^{\frac{1}{2}}) J_0(2\lambda_n z^{\frac{1}{2}}) - J_0(2\lambda_n z_o^{\frac{1}{2}}) Y_0(2\lambda_n z^{\frac{1}{2}})] dz$$

$K_{n1}$ ,  $K_{n2}$  and  $E_n$  are functions of the eigenvalues,  $\lambda_n$ .

Figure 2.3 shows the relative contributions from each of the shear stress terms in (2.58). The first term has the form of a quadratic stress law but also contributes a negligible fraction (about 1/100) of the total bed stress when  $d \gg z_o$  (see the third panel of Figure 2.3). As with the Case 1 and 2, the second term reduces to a quadratic stress law when only the first eigenvalue and  $\sigma = t$  condition are considered (see forth panel of Figure 2.3). Unlike Case 2, the integral in the third term cannot be simply described under the same assumptions. When more eigenvalues are included and the convolution integral is completed, the second term results in a phase lead relative to the free stream velocity, but the third term predicts a phase lag. The third term contributes about 1/5 of the total bed stress. The total bed stress predicts a phase lead relative to the free stream velocity.

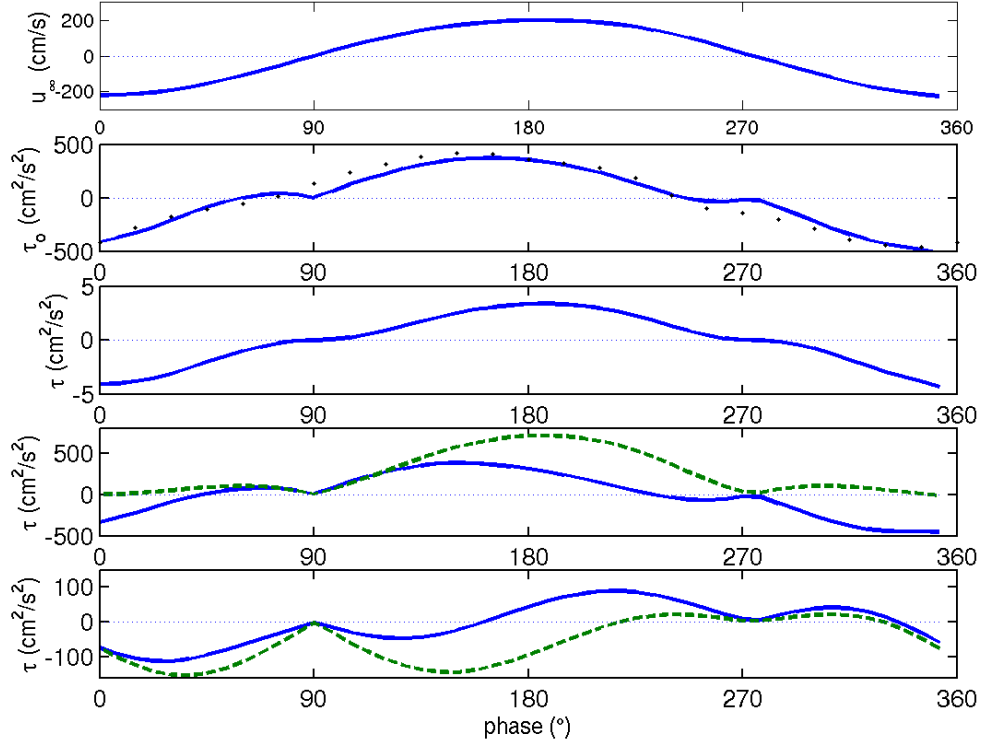


Figure 2.3: Bed shear stress contributions for the temporally and spatially varying eddy viscosity (Case 3). The top panel presents the free stream velocity, the second panel presents the predicted bed stress (solid line), and the bed stress measured by Jonsson and Carlsen (1976) (dots). The bottom 3 panels present the first (second panel), second (third panel), and third (bottom panel) terms of the predicted bed stress for the 15 eigenvalues (solid line) and the first eigenvalue ( $\sigma = t$ ) condition (dashed line) solutions.

## CHAPTER 3

### CALIBRATION AND EVALUATION OF THE WAVE BOTTOM BOUNDARY LAYER MODEL

Each of the three model solutions presented in Chapter 2 have a single free parameter ( $R_1$ ,  $R_2$ , and  $R_3$ ). Since the bed load sediment transport models are highly dependent on the bed shear stress, the calibration of the free parameter will be performed with bed stresses inferred from laboratory observations of horizontal velocities by Jonsson and Carlsen (1976). Following model calibration, each of the 3 model solutions will be evaluated with the laboratory observations by Jonsson and Carlsen (1976) and Jensen *et al.* (1989), and the observations from Duck94 field experiments.

#### **3.1 Model calibration and evaluation with observations by Jonsson and Carlsen (1976)**

Both beach scale energetics based and boundary layer scale bed load sediment transport models are highly dependent on the shear stress applied to the bed. Because it is not yet possible to directly measure the bed load sediment transport, the wave bottom boundary layer model is calibrated by comparing the bed stress predictions with the laboratory observations by Jonsson and Carlsen (1976).

Jonsson and Carlsen (1976) measured the temporal and vertical structure of the oscillatory bottom boundary layer within an oscillating U-tube. The water level in the

	msd ( $cm^2/s^2$ )
$R_1=4.4$	147.1
$R_1=4.5$	145.5
$R_1=4.6$	148.2
$R_2=0.4$	91.7
$R_2=0.5$	47.7
$R_2=0.6$	55.0
$R_3=0.07$	82.8
$R_3=0.08$	64.2
$R_3=0.09$	72.2

Table 3.1: Root-mean-square-deviations (msd) between the model predicted stresses and the measurements in the best-fit analysis.

open riser of the U-tube was recorded simultaneously with the velocity measurements. The velocity amplitude was 200 cm/s, the period was 8.39 sec, and the bed level was 0.077 cm. With a best-fit analysis (see Table 3.1), the free coefficients in the analytical bottom boundary layer model are  $R_1 = 4.5$  in Case 1,  $R_2 = 0.5$  in Case 2, and  $R_3 = 0.08$  in Case 3. The coefficients are assumed constant in the following simulations.

Figure 3.1 shows the predicted shear stresses compared with the measured shear stress by Jonsson and Carlsen (1976). Along with the three cases of the bottom boundary layer model, the quadratic stress law (1.9) is also included in the comparison. The shear stresses predicted by the constant eddy viscosity model (Case 1) and the spatially varying eddy viscosity model (Case 2) have phase leads, compared with the observations, while those from the temporally and spatially varying eddy viscosity model (Case 3) and the quadratic stress law have phase lags. The correlation coefficient, root-mean-square-deviation (msd), and phase differences are given in Table

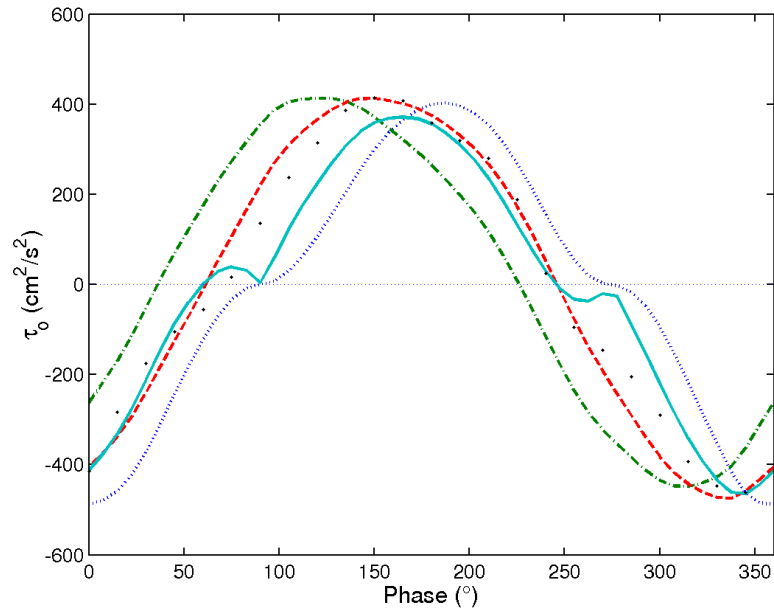


Figure 3.1: Bed shear stress comparisons between the predicted values from Case 1 (dashed with dots), Case 2 (dashed), Case 3 (solid), and the quadratic stress law, and measured values by Jonsson and Carlsen (1976) (dots).

3.2. The statistical results in Table 3.2 show that the spatially varying eddy viscosity (Case 2) and the spatially and temporally varying eddy viscosity (Case 3) boundary layer models perform better than the constant eddy viscosity model (Case 1) and the quadratic stress law. The time-varying eddy viscosity model (Case 3) does not result in the lower msd, however it does yield a phase difference of less than  $10^\circ$ .

Figure 3.2 shows the velocity comparisons between model simulations and measurements by Jonsson and Carlsen (1976) at the peak horizontal velocity condition ( $\theta = 180^\circ$  in Figure 3.3). As displayed in Table 3.3, the correlations of peak horizontal velocity between each of the models and the data are very high. The msd of peak horizontal velocities between the depth varying eddy viscosity models (Case 2

	Case 1	Case 2	Case3	BBB
$R^2$	0.78	0.98	0.96	0.80
msd( $cm^2/s^2$ )	145.5	47.67	64.16	134.48
$\Delta\theta(^{\circ})$	33	19.5	-9	-30

Table 3.2: Statistical comparisons of the predicted bed stresses of the bottom boundary layer models, Case 1, Case 2, and Case 3, and the BBB ( $c_f = 0.01$ ) models with laboratory observations by Jensen *et al.* (1989).  $R^2$ , msd, and  $\Delta\theta$  indicate the correlations, root-mean-square-deviations, and phase differences between the model predicted bed stresses and the measurements.

	Case 1	Case 2	Case 3
$R^2$	0.988	0.983	0.986
msd (cm/s)	39.0	8.94	9.28

Table 3.3: Statistical comparisons of the predicted peak velocities of Case 1, Case 2 and Case 3 with laboratory observations by Jonsson and Carlsen (1976).  $R^2$  and msd indicate the correlations and the root-mean-square-deviations between the model predicted peak velocities and the observations.

and Case 3) and the observations are small (less than 10 cm/s). The constant eddy viscosity model (Case 1) is an exception with a msd of 39.05 cm/s.

The temporal and spatial variability of the models are evaluated in Figure 3.3 and Figure 3.4, respectively. The temporal variability of the models is evaluated by computing the vertical rms and vertical msd of the horizontal velocity over the measurement array at each time, Figure 3.3. These comparisons show that the velocity predictions from the spatially varying eddy viscosity models (Case 2 and Case 3) compare well with the observations. The largest deviation exists in the constant eddy

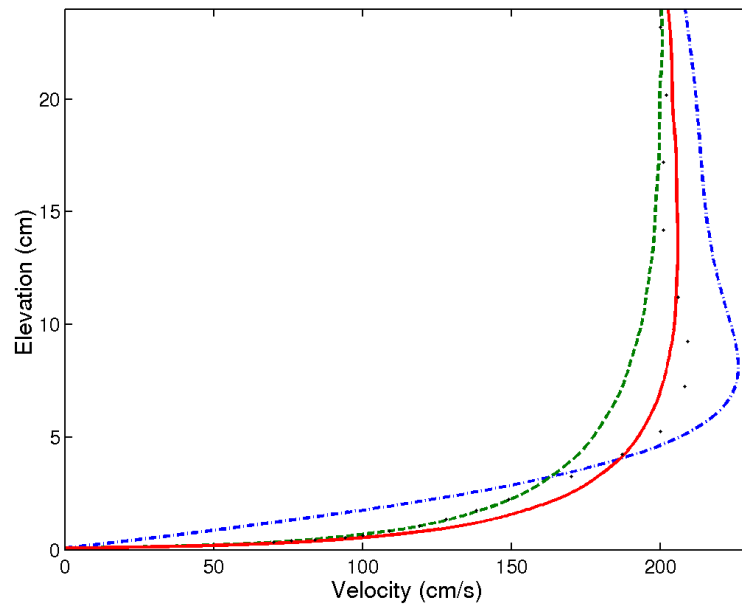


Figure 3.2: Comparisons between the predicted peak horizontal velocities of Case 1 (dashed with dots), Case 2 (dashed) and Case 3 (solid), and the observations by Jonsson and Carlsen (1976) (dots) at the peak velocity ( $\theta = 180^\circ$  in Figure 3.3).

viscosity model (Case 1). The larger deviations occur at  $90^\circ - 150^\circ$  and  $270^\circ - 330^\circ$  in Case 2 and Case 3.

The spatial variability of the models is evaluated by computing the temporal rms and msd of the horizontal velocity at each vertical elevation, Figure 3.4. The constant viscosity model (Case 1) significantly under predicts the horizontal velocity through out the entire wave bottom boundary layer, and is generally unacceptable. The largest msd occurs at middle elevation in the spatially varying eddy viscosity model (Case 2), and at lower elevation in the temporally and spatially varying eddy viscosity model (Case 3). The comparisons imply good performances of the spatially varying eddy viscosity models (Case 2 and Case 3) in velocity predictions, but the temporally varying eddy viscosity model (Case 3) shows better performance in the shear stress phase difference predictions.

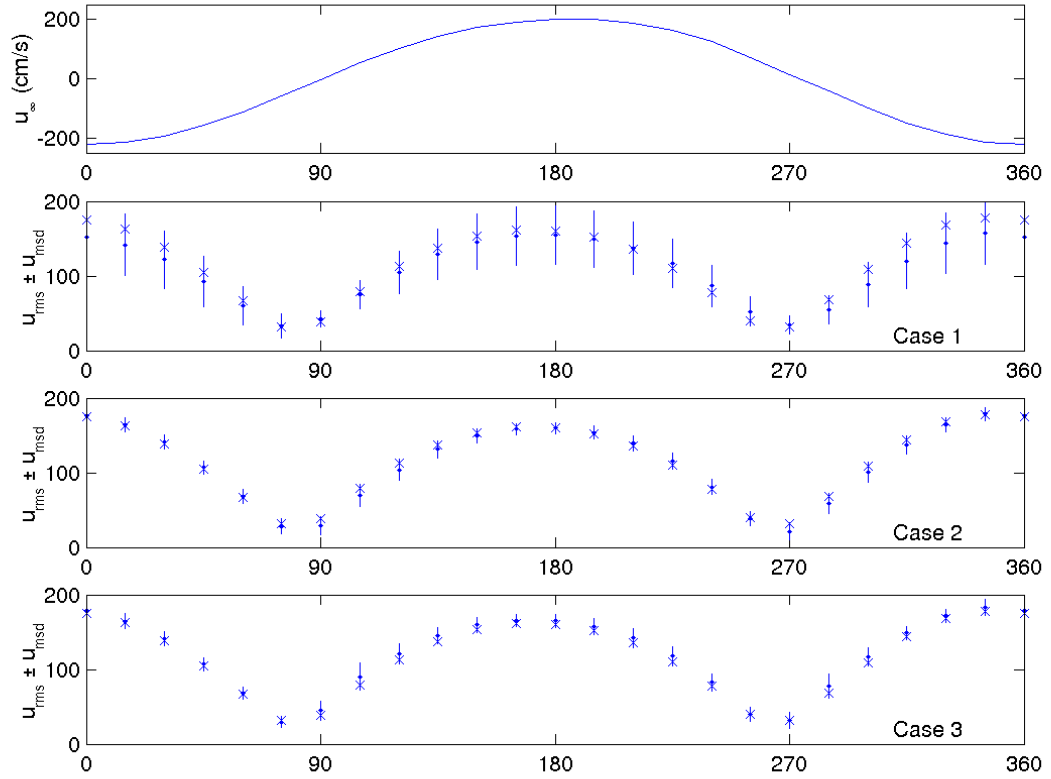


Figure 3.3: Comparisons of the rms horizontal velocity ( $u_{rms}(\theta)$ ) calculated over the elevation at each wave phase for the Jonsson and Carlsen (1976) case. The top panel presents the free stream velocity, the bottom three panels present the bottom boundary layer models, Case 1, Case 2 and Case 3. ( $\cdot$ ) indicates the model results and ( $\times$ ) indicates observations by Jonsson and Carlsen (1976). Errorbars indicate  $\pm$  one root-mean-square-deviation ( $u_{msd}(\theta)$ ) between the model results and observations.

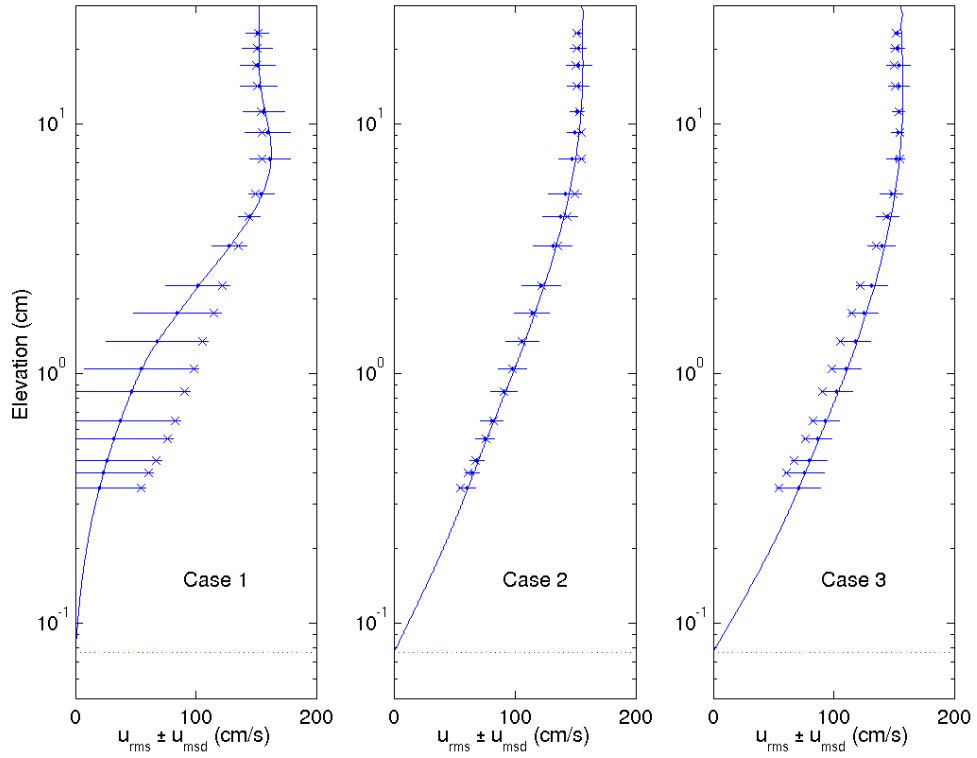


Figure 3.4: Comparisons of the rms horizontal velocity ( $u_{rms}(z)$ ) calculated over the wave phase at each elevation for Case 1, Case 2 and Case 3 (left to right panels, respectively) for the Jonsson and Carlsen (1976) case. ( $\cdot$ ) indicates the model results and ( $\times$ ) indicates observations by Jonsson and Carlsen (1976). Errorbars indicate  $\pm$  one root-mean-square-deviation ( $u_{msd}(z)$ ) between the model results and observations. The dashed lines indicate the bed level,  $z_o$ .

### 3.2 Model evaluation with observations by Jensen *et al.* (1989)

The models are also evaluated with the more recent laboratory observations of Jensen *et al.* (1989). A purely oscillating flow with sinusoidal velocity variation was used for the oscillatory boundary layer study. The wave amplitude is 100 cm/s, the wave period is 9.27 sec, and the bed level is 0.0028 cm. Both the stream-wise and vertical velocities were measured in the experiments.

The temporal and spatial variability of the models is evaluated in Figure 3.5 and Figure 3.6. The comparisons show similar tendencies as the comparisons with Jonsson and Carlsen's observations (1976). In the comparisons at each phase (Figure 3.5), the spatially varying eddy viscosity models (Case 2 and Case 3) are consistent with the observations, with the biggest deviation existing in the constant eddy viscosity model (Case 1). Also consistent with the previous comparisons, the temporally and spatially varying eddy viscosity model (Case 3) yields better performance at lower free stream velocities ( $0 - 45^\circ$ ). Evaluation of the spatial variability of the models shows the largest deviations also exist in Case 1 (Figure 3.6). The model over predicts the vertical variability of the horizontal velocity and significantly under predicts the near bed velocity. The largest msd occurs in the middle elevation in Case 2, and at the lower elevation in Case 3.

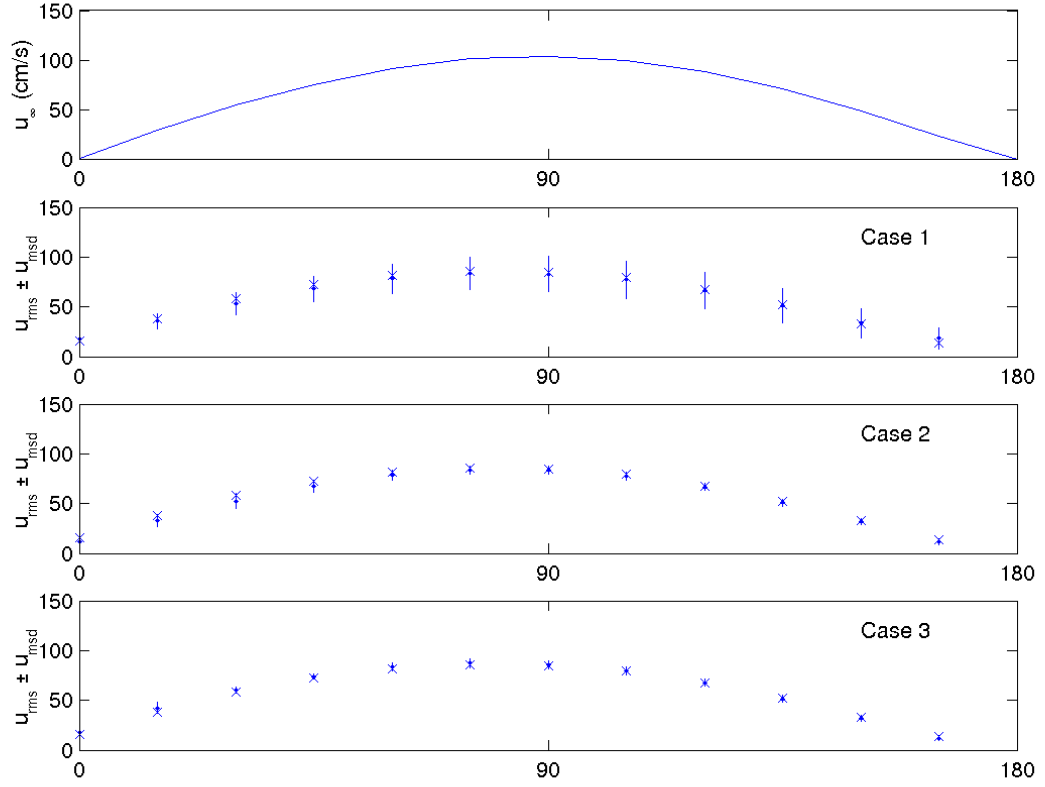


Figure 3.5: Comparisons of the rms horizontal velocity ( $u_{rms}(\theta)$ ) calculated over the elevation at each wave phase for the Jensen *et al.* (1989) case. The top panel presents the free stream velocity, the bottom three panels present the bottom boundary layer models, Case 1, Case 2, and Case 3. ( $\cdot$ ) indicates the model results and ( $\times$ ) indicates observations by Jensen *et al.* (1989). Errorbars indicate  $\pm$  one root-mean-square-deviation ( $u_{msd}(\theta)$ ) between the model results and observations.

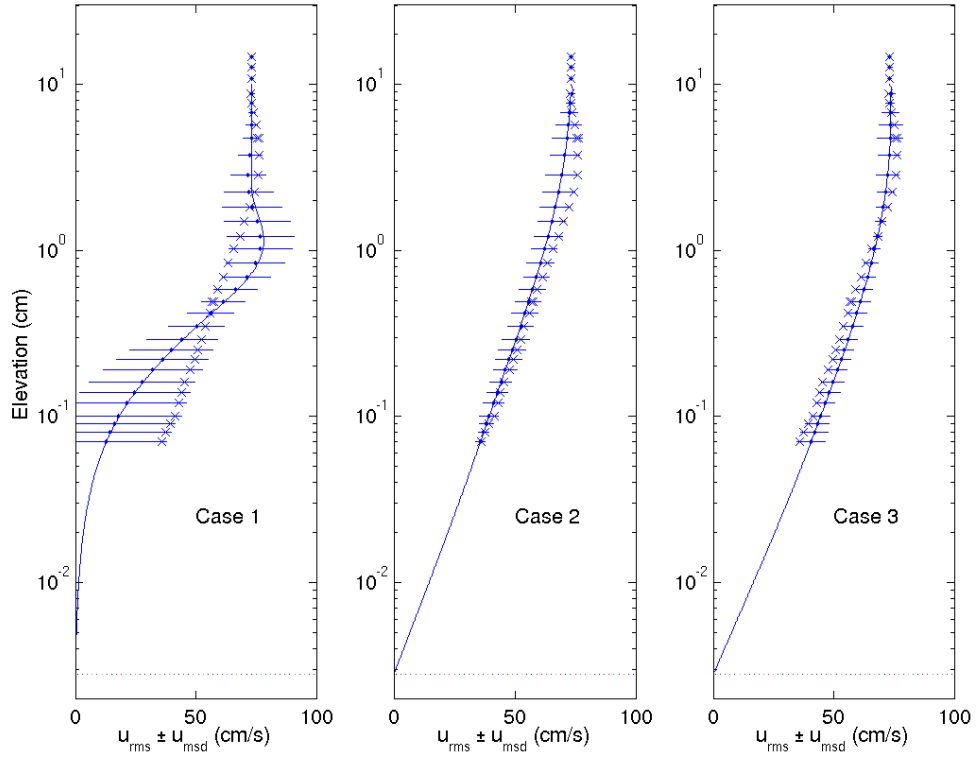


Figure 3.6: Comparisons of the rms horizontal velocity ( $u_{rms}(z)$ ) calculated over the wave phase at each elevation for Case 1, Case 2 and Case 3 (left to right panels, respectively) for the Jensen *et al.* (1989) case. ( $\cdot$ ) indicates the model results and ( $\times$ ) indicates observations by Jensen *et al.* (1989). Errorbars indicate  $\pm$  one root-mean-square-deviation ( $u_{msd}(z)$ ) between the model results and observations. The dashed lines indicate the bed level,  $z_o$ .

### 3.3 Model evaluation with Duck94 field observations

The final model evaluation of the eddy viscosity schemes is performed with field observations of the wave bottom boundary layer. The field observations were made at the Army Corps of Engineers, Field Research Facility in Duck, NC from 14 Aug 94 to 23 Aug 94 as part of the cooperative Duck94 experiment (Foster *et al.*, 2000). During the experiment the wave bottom boundary layer velocity observations were made with a vertical array of five hot film anemometers, in the lower 5 cm of the water column with a 1 cm array spacing. The wave bottom boundary layer models established in the thesis are evaluated with a particular 256 sec velocity time series under flat bed conditions with a 0.53 m/s free stream velocity amplitude and 5.36 sec wave period. The normalized wave skewness is 0.04 and the asymmetry is 0.14.

Figure 3.7 shows a 30 sec time series of the free stream velocity (top panel), and the corresponding time-varying bed shear stress comparisons between the observations and the predictions (bottom panel). For the field observation, the bed shear stress is estimated based on the bottom boundary layer velocity profile (see Appendix A). Considering the uncertainty of the elevation of the instrument array relative to the true bed level, the estimates of observed bed stress may exhibit considerable variability. Consequently, the bed stress has also been estimated for the uppermost and the lowermost locations of the instrument array (see shaded area of the bottom panel in Figure 3.7). The bed stresses from the spatially varying eddy viscosity models (Case 2 and 3) are mostly within the upper and lower limits of bed stress. Following Foster *et al.* (2000), the bed level  $z_o = 0.08$  cm and upper boundary  $d = 14$  cm are assumed in the analytic model simulations. The statistical comparison coefficients are given in Table 3.4. The correlation coefficient between observations and model

	Case 1	Case 2	Case 3
$R^2$	0.48	0.79	0.90
$\text{msd}(cm^2/s^2)$	44.9	16.4	14.6
$\text{msd}(-\Delta z)(cm^2/s^2)$	50.7	29.6	32.5
$\text{msd}(+\Delta z)(cm^2/s^2)$	57.2	30.9	19.9

Table 3.4: Statistical comparisons of the predicted bed stresses by the bottom boundary layer models, Case 1, Case 2, and Case 3 with observations from the Duck94 field experiment.  $\pm\Delta z$  means bed level measurement error is considered.  $R^2$  and msd indicate the correlation coefficients and root-mean-square-deviations between the model predicted bed stresses and the Duck94 field observations.

predictions by the temporally varying eddy viscosity model (Case 3) is higher than the temporally constant eddy viscosity models (Case 1 and Case 2), and the msd of the spatially varying eddy viscosity models (Case 2 and Case 3) are small, which means the temporally varying eddy viscosity model (Case 3) performs best. Consistent with the comparisons with laboratory observations, the bed stress predicted by both Case 2 and Case 3 result in the highest model skill.

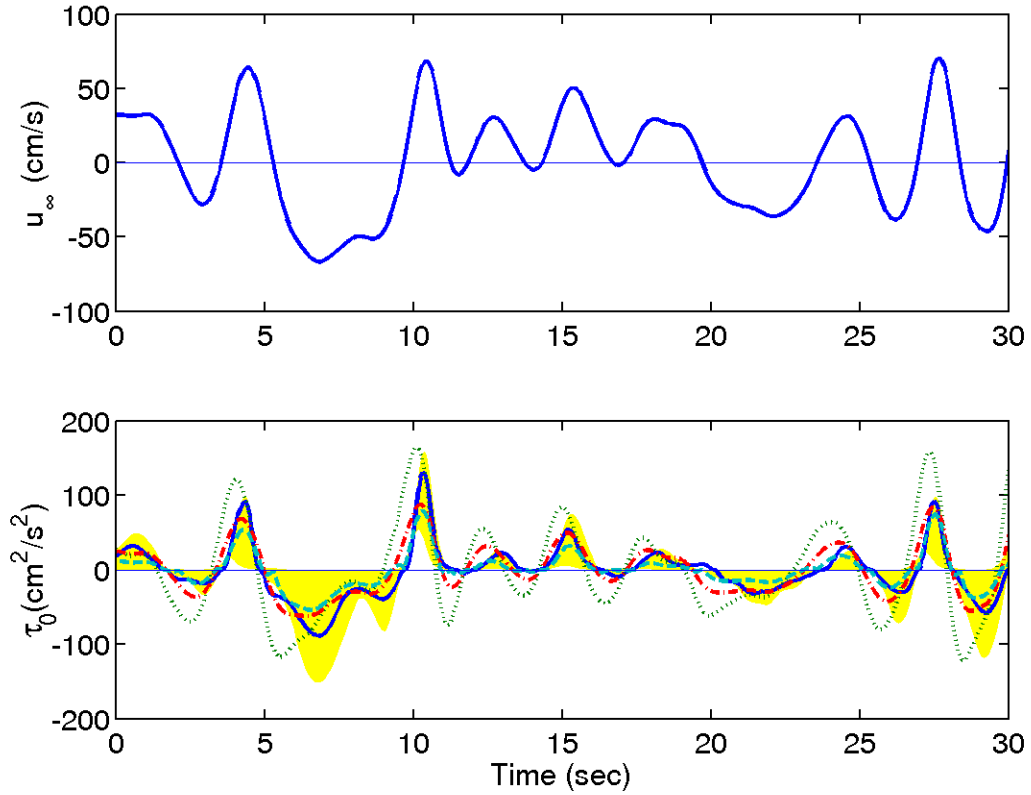


Figure 3.7: A 30 sec time series of the free stream velocity (top) and the corresponding bed shear stresses comparisons (bottom) between the predictions from the bottom boundary layer models, Case 1 (dotted), Case 2 (dashed with dots), and Case 3 (dashed), and the field observations (solid). Shade area indicates the lower and upper boundary of the bed stress estimation when bed level measurement error is considered. Positive denotes onshore direction.

## CHAPTER 4

### SEDIMENT TRANSPORT MODEL EVALUATIONS

An energetics based bed load transport model and the empirical models of Meyer-Peter and Müller (1948) and Engelund and Fredsøe (1976) are formulated with the analytical bed shear stress predictions derived in Chapter 2. All the three bed load models are compared and evaluated with the discrete particle simulations of Drake and Calantoni (2001). The models are examined with waveforms containing varying skewness and asymmetry.

#### 4.1 Simulated waveforms

A sinusoidal and three non-linear waveforms are considered in the model evaluations. The waveforms have a constant peak period of  $T = 6$  sec and maximum free stream velocity amplitudes of 0.5, 0.75, 1.0, 1.25, and 1.5 m/s. The time-varying pressure gradient force exerted on the sediment,  $\frac{dp}{dx}$ , is assumed to be proportional to

$$\frac{dp}{dx} \propto \sum_{i=0}^4 \frac{1}{2^i} \sin[(i+1)\omega t + i\phi] \quad (4.1)$$

where  $\omega = 2\pi/T$  is the angular wave frequency, and  $\phi$  is phase shift corresponding to those of Drake and Calantoni (2001). Drake and Calantoni (2001) defined the force on the individual grains to be proportional to the pressure gradient, but did not

include a boundary layer solution for the water column flow. Figure 4.1 shows the free stream velocity time series for the sinusoidal and the three non-linear waveforms having  $\phi = 0, \pi/4,$  and  $\pi/2$ , in which the maximum horizontal velocity is 1.0 m/s. Increasing  $\phi$  in the non-linear waves corresponds to increasing the wave asymmetry which commonly happens as waves evolve from shoaling to breaking. The sawtooth waveform ( $\phi = \pi/2$ ) is characteristic of surf zone bores. The skewness (S) and asymmetry (A) of the waves are shown in Table 4.1.

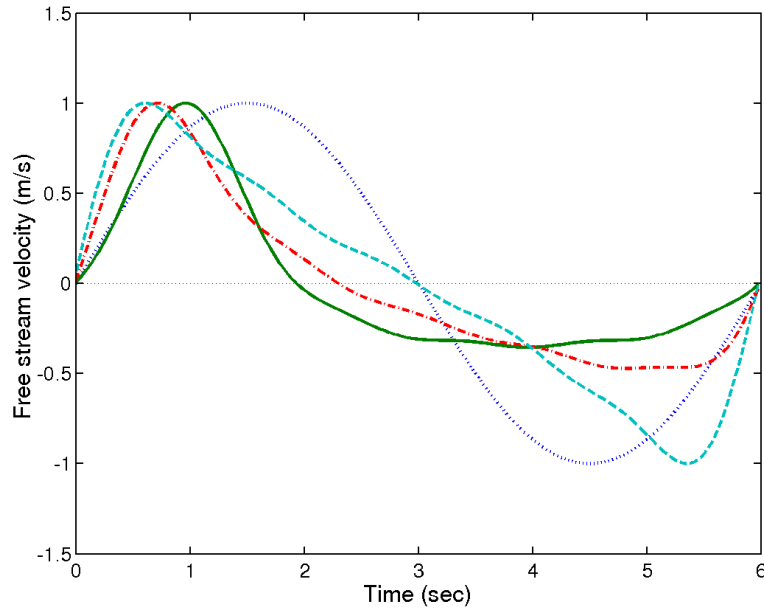


Figure 4.1: Waveforms for the sinusoidal (dotted), skewed ( $\phi = 0$ , solid line), combined ( $\phi = \pi/4$ , dashed line with dots), and asymmetric ( $\phi = \pi/2$ , dashed line) waves, with a 6 sec wave period and a 1.0 m/s maximum fluid velocity. Onshore directed flow is positive.

	Sinusoidal	Skewed	Combined	Asymmetric
Skewness	0	1.2	0.85	0
Asymmetry	0	0	0.85	1.2

Table 4.1: Skewness and asymmetry of the waveforms.

All of the bed load sediment transport models are strongly dependent on the bed shear stress. Consequently, the predicted bed stresses under each wave condition are first compared against the traditional quadratic stress law. Figure 4.2 shows the bed shear stress comparisons under the sinusoidal, skewed ( $\phi = 0$ ), combined ( $\phi = \pi/4$ ), and asymmetric ( $\phi = \pi/2$ ) wave conditions. The friction factor,  $c_f$ , is taken to be 0.01 as calibrated in Chapter 3. In all models, the rms bed shear stress increases with increasing wave amplitude. The quadratic stress law predicts higher rms bed stress than the three analytical models.

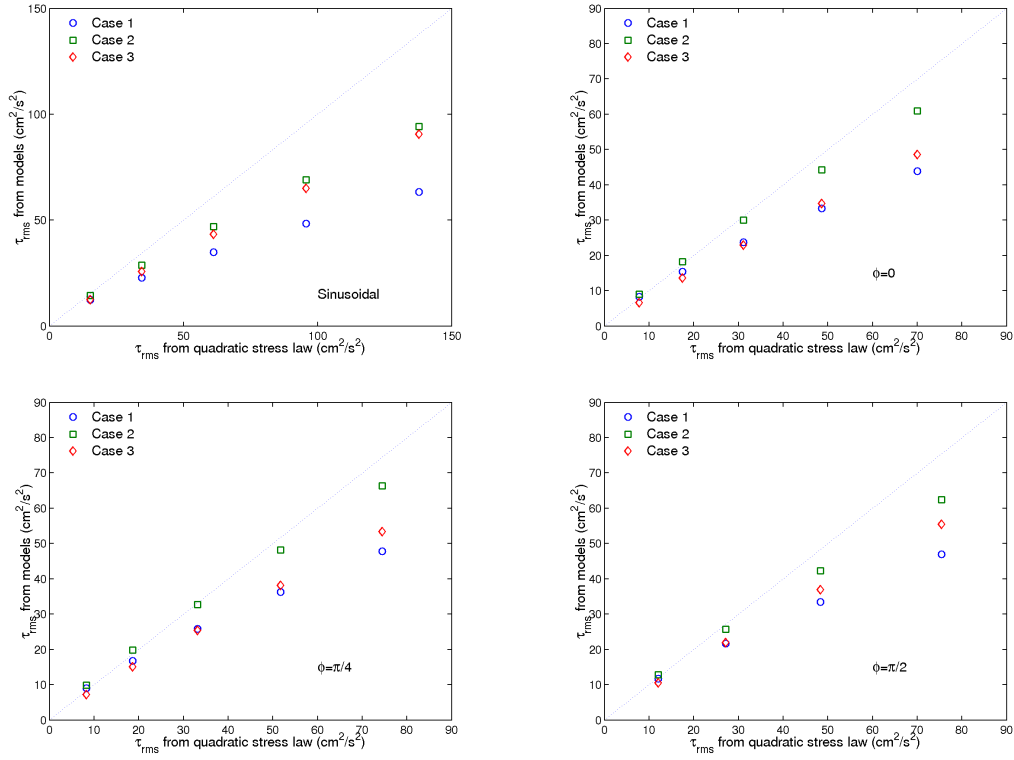


Figure 4.2: Comparisons of the rms of the bed shear stresses predicted by the bottom boundary layer models, Case 1 (squares), Case 2 (pluses), and Case 3 (diamonds) with the quadratic stress law ( $c_f = 0.01$ ) (x-coordinate) under sinusoidal, skewed ( $\phi = 0$ ), combined ( $\phi = \pi/4$ ), and asymmetric ( $\phi = \pi/2$ ) wave conditions.

## 4.2 Time-varying sediment flux comparisons

First, the response of the models to a sinusoidal wave with a 1.0 m/s amplitude and a 6 sec period is examined. Figure 4.3 shows the time-varying sediment fluxes predicted by the energetics model, the Engelund and Fredsøe (1976) and the Meyer-Peter and Müller (1948) models. The bed load efficiency assumed for the energetics based flux predictions is  $\epsilon_b = 0.21$ , following Bailard (1981). The drag coefficient assumed for the quadratic stress law (1.9) is  $c_f = 0.01$ . The sediment grain size,  $d_{50}$ , was 1.1 mm. In the comparisons, the traditional quadratic stress law results in significantly higher time-varying sediment fluxes by the E-F and MP-M models. The constant eddy viscosity model (Case 1) results in lower sediment flux amplitudes and larger phase differences between the bed stress and the free stream velocity than either of the spatially varying eddy viscosity models (Case 2 and Case 3). The two spatially varying eddy viscosity models (Case 2 and 3) predict similar local maxima of the time-varying sediment flux and phase differences. The energetics based models predict lower peak amplitudes (ie. 0.5 kg/m/s for Case 3) than the Engelund and Fredsøe (1976) model (ie. 0.65kg/m/s for Case 3) and the Meyer-Peter and Müller (1948) model (ie. 0.6kg/m/s for Case 3). The net fluxes from all the models are negligible ( $\sim 0.0001$  kg/m/s).

Predictions of bed stress by the three analytical wave bottom boundary layer models and the quadratic stress law are used to examine the time-varying sediment flux for the non-linear waveforms discussed in section 4.1. Similarly, the three bed load sediment flux models are considered for each of the three analytical bed stress predictions and the quadratic stress law. Intra model comparisons are performed for a purely skewed wave ( $\phi = 0$ ), a combined wave ( $\phi = \pi/4$ ), and a purely asymmetric

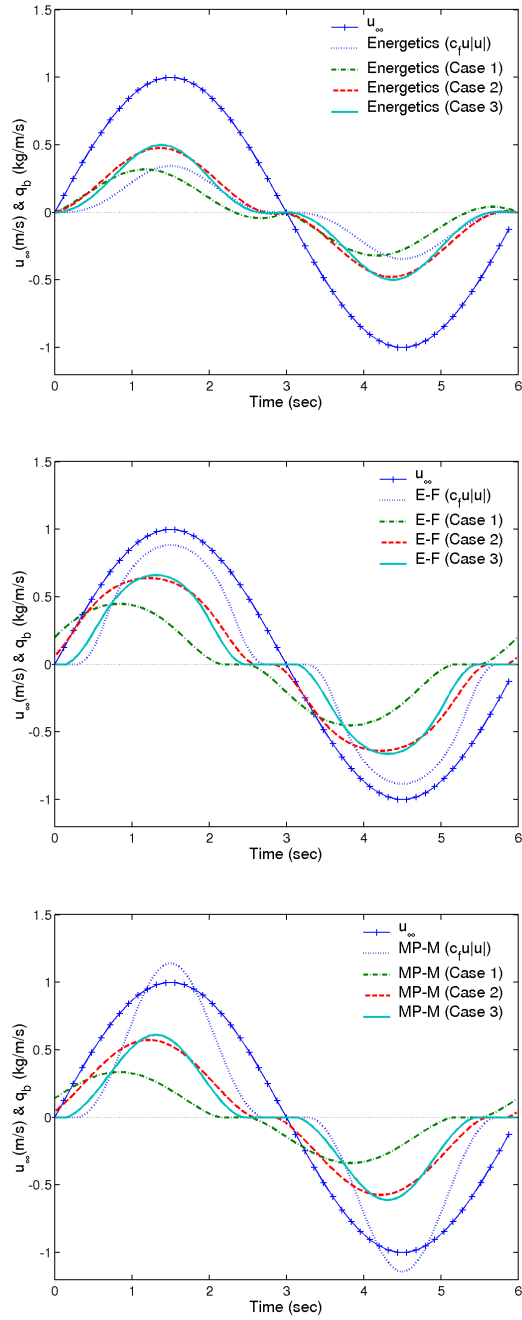


Figure 4.3: Comparisons of the predicted time-varying sediment flux by energetics based (top panel), E-F (middle panel), and MP-M (bottom panel) bed load sediment transport models under a sinusoidal wave condition.

wave ( $\phi = \pi/2$ ). The model predictions are qualitatively evaluated with the discrete particle simulations of Drake and Calantoni (2001).

Figure 4.4 shows the time-varying sediment fluxes predicted by the energetics based, the E-F, and the MP-M models under a purely skewed wave condition ( $\phi = 0$ ). The peak amplitudes of  $q_b$  predicted by the quadratic stress law are higher than the analytical methods in the MP-M and E-F models. As the quadratic stress law does not include the phase difference between the bed stress and velocity, the sediment flux has the same phase as the free stream velocity,  $u_\infty$ . The predicted time-varying bed load flux from all analytical models leads the free stream velocity. The constant eddy viscosity model (Case 1) results in the largest phase lead of approximately  $20^\circ$ . Results from the spatially varying eddy viscosity models (Case 2 and Case 3) lead the free stream velocity by approximately  $10^\circ$ . The peak value predicted from the energetics based model ( $0.4 - 0.5$  kg/m/s), the E-F model ( $0.5 - 0.7$  kg/m/s), and the MP-M model ( $0.45 - 0.7$  kg/m/s) with the analytical bed stress formulations are comparable with the discrete particle simulations ( $0.6$  kg/m/s). The peaks of the predicted sediment flux from the energetics based model (top panel) are lower than those found with the other two models (middle panel and bottom panel of Figure 4.4). The constant eddy viscosity model (Case 1) predicts a lower sediment flux peak than the spatially varying eddy viscosity models (Case 2 and Case 3).

Figure 4.5 shows the comparisons of the predicted time-varying bed load sediment flux from each sediment transport model under the combined wave condition ( $\phi = \pi/4$ ). Similar to the comparisons under the skewed wave condition, the quadratic stress law predictions have the same phase as the free stream velocity and the highest flux peak values in the MP-M and E-F models. Flux predictions from the other

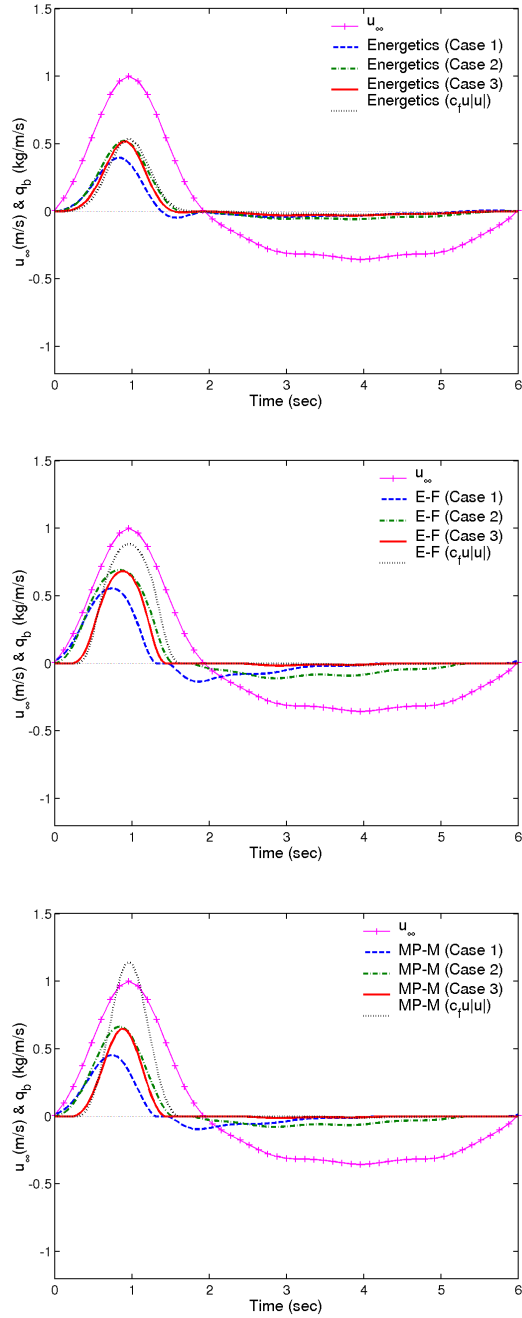


Figure 4.4: Comparisons of the predicted time-varying sediment flux by energetics based (top panel), E-F (middle panel), and MP-M (bottom panel) bed load sediment transport models under skewed wave condition ( $\phi = 0$ ).

models have a phase lead compared with velocity, in which again the largest phase lead exists in the constant eddy viscosity model (Case 1). The peak values predicted from the energetics based model (0.4–0.5 kg/m/s), the E-F model (0.5–0.75 kg/m/s), and the MP-M model (0.6 – 0.75 kg/m/s) with the analytical stress formulations are lower compared with the the discrete particle simulations(0.8 kg/m/s). The energetics based model (top panel) predicts lower flux peak values than the other two models. The constant eddy viscosity model (Case 1) predicts a lower local maximum flux than the spatially varying eddy viscosity model (Case 2 and Case 3) in all comparisons.

Figure 4.6 shows the comparisons of time-varying bed load sediment flux predictions under a purely asymmetric wave condition ( $\phi = \pi/2$ ). The phase differences are similar to the other waveforms. The energetics based model (top panel) predicts a lower local maximum flux than other two models. Since the asymmetric wave has the same onshore and offshore wave amplitude and shape, the quadratic stress law predicts the same amplitude of onshore and offshore sediment flux, therefore the net flux is zero. With the exception of the quadratic stress law, all the other model predictions have a higher onshore flux amplitude, thus producing an onshore directed net flux. The peak values predicted from the energetics based model (0.45 – 0.6 kg/m/s), the E-F model (0.75 – 0.8 kg/m/s), and the MP-M model (0.8 – 0.9 kg/m/s) with the analytical bed stress formulations are lower than the discrete particle simulations (1.0 kg/m/s). However the peak values predicted by the E-F and MP-M models with quadratic stress law assumption are comparable to the discrete particle simulations. In the energetics based model comparison (top panel of Figure 4.4 - Figure 4.6), the constant eddy viscosity model (Case 1) results in a lower amplitude in the both onshore and offshore directions than the spatially varying eddy viscosity models (Case

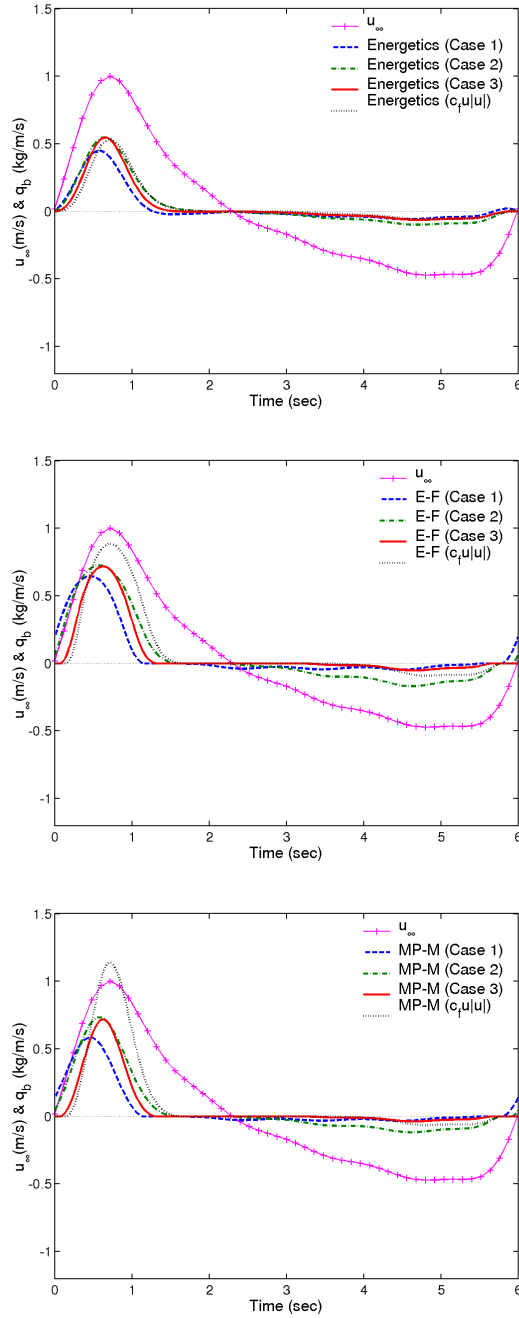


Figure 4.5: Comparisons of the predicted time-varying sediment flux by energetics based (top panel), E-F (middle panel), and MP-M (bottom panel) bed load sediment transport models under combined wave condition ( $\phi = \pi/4$ ).

2 and Case 3). In the E-F and the MP-M simulations (middle panel of Figure 4.4 - Figure 4.6), the onshore flux from the constant eddy viscosity model (Case 1) has comparable amplitude with those from the spatially varying eddy viscosity models (Case 2 and Case 3), but the offshore fluxes are lower.

From the above comparisons, unlike the linear wave, almost all net sediment fluxes are onshore directed. This is consistent with the results predicted with the discrete particle simulations of Drake and Calantoni (2001). The time-varying sediment flux peaks predicted by the models with the analytical stress formulations are generally lower than those predicted by the discrete particle simulations. The energetics based model predicts lower time-varying sediment fluxes than the E-F and MP-M models. However, a linear increase in the bed load efficiency parameter would result in a linear increase prediction of the instantaneous flux in the energetics based models.

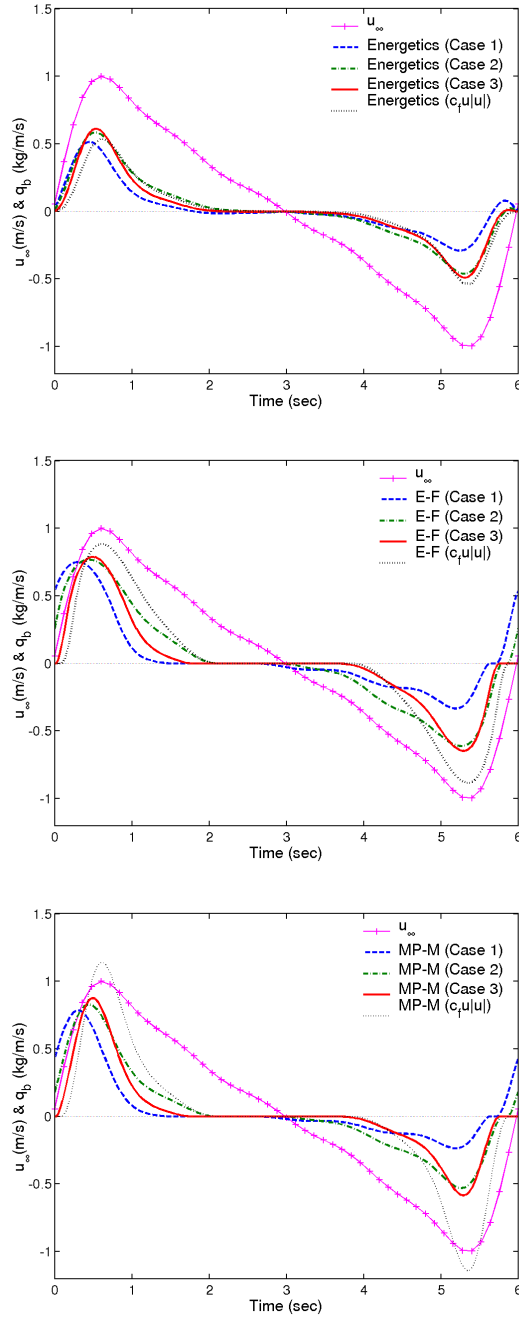


Figure 4.6: Comparisons of the predicted time-varying sediment flux by energetics based (top panel), E-F (middle panel), and MP-M (bottom panel) bed load sediment transport models under asymmetric wave condition ( $\phi = \pi/2$ ).

### 4.3 Time-averaged sediment flux comparisons

In this section, discussions focus on the comparisons of the predicted time-averaged sediment transport for the three non-linear waveforms. The time-averaged sediment fluxes are compared to the discrete particle simulations of Drake and Calantoni (2001) and the modified BBB model (1.12) by Drake and Calantoni (2001).

Figure 4.7 shows the time-averaged bed load sediment flux predictions for a purely skewed wave condition ( $\phi = 0$ ). The discrete particle simulations of Drake and Calantoni (2001), as well as the modified BBB model by Drake and Calantoni (2001), are compared with the energetics based model, the E-F model, and the MP-M model for each analytical solution. All predicted sediment fluxes are in the onshore direction. The time-averaged bed load sediment fluxes from the energetics based model (top panel) and the MP-M model (bottom panel) increase with increasing wave amplitude. However, the E-F model (middle panel) reaches a local maximum when the wave amplitude exceed 1.25 m/s. The modified BBB model by Drake and Calantoni (2001) is calibrated with the discrete particle simulations and consequently results in a similar amplitude. The energetics based models from the analytical boundary layer models (Case 1, Case 2, and Case 3) and the quadratic stress law predict less flux than the discrete particle simulations (about 30% - 60%) for a bed load efficiency parameter of 0.21, but the results of the MP-M and E-F models with quadratics stress law assumption are higher than the discrete particle simulations. The E-F model diverges from the discrete particle simulations as the wave amplitude increases. This may be caused by increasing contributions from the offshore directed flux as the wave amplitude increases. With the exception of the constant eddy viscosity model

(Case 1) and the quadratic stress law, the time-averaged flux predictions from MP-M model with the analytical bed stress formulations are very close to the discrete particle simulations (about 70% - 90%). However MP-M model with the quadratics stress formulation can predict near two times of the result from the discrete particle simulations. To highlight the sensitivity of the energetics based model to the bed load efficiency parameter,  $\epsilon_b$ , the top panel in Figure 4.7 shows the range of predicted fluxes for the range of bed load efficiencies ( $0.13 < \epsilon_b < 1.03$ ) found in available literatures (Drake and Calantoni, 2001; Bagnold, 1966). The amplitudes could also be increased by increasing the drag coefficient,  $c_f$  (Hsu *et al.*, 2004).

Figure 4.8 shows the time-averaged bed load sediment flux predictions for the combined wave condition. With  $\epsilon_b = 0.21$ , the energetics based model can only predict 20% – 50% of the flux from the discrete particle simulations. Similar to the skewed wave ( $\phi = 0$ ) condition, the predictions from the E-F model show maximum sediment flux at a wave amplitude of 1.25 m/s. The MP-M models with analytical bed stress formulations (bottom panel) again predict the sediment flux with estimations nearing about 50% – 80% of those obtained with the discrete particle simulations, but with the quadratics stress formulation predict nearly two times of the results from the discrete particle models. The ranges of predicted fluxes for the range of bed load efficiencies ( $0.13 < \epsilon_b < 1.03$ ) are shown in the top panel.

Figure 4.9 shows the time-averaged bed load sediment flux predictions for the asymmetric wave condition. Compared with the skewed ( $\phi = 0$ ) and combined ( $\phi = \pi/4$ ) waves, the time-averaged sediment fluxes are lower under the asymmetric ( $\phi = \pi/2$ ) waves. As the wave amplitude and shape are the same in the onshore and offshore directions, the quadratic stress law predicts zero time-averaged flux for all three bed

load models. The energetics based model assuming one of the three analytical bed stresses (Case 1, 2 and 3) can predict only 30% of the flux from the discrete particle simulation flux. Even increasing the bed load efficiency to 1.03, the energetics based model would still result in an under prediction of the time-averaged bed load flux. The predictions from the E-F model have local maxima at a wave amplitude of 1.0 m/s. The MP-M model with the analytical bed stress formulations predict relatively closer results compared with the discrete particle simulations (about 50% – 90%).

The energetics based bed load sediment transport model and the MP-M model predict increasing time-averaged sediment fluxes when wave amplitude increases, while the predictions from the E-F model have a tendency to predict a local maximum at a wave amplitude of 1.00 – 1.25 m/s. Energetics based models can predict only 20% – 60% of the time-averaged flux of the discrete particle simulations with the percentage decreasing with the increasing of  $\phi$  (from skewed wave to asymmetric wave) when  $\epsilon_b = 0.21$ . Given that the flux by the energetics based model is linear dependent on the bed load efficiency, the predictions increase with increasing bed load efficiency. However, the energetics based model would still result in an underprediction of the time-averaged bed load flux compared with the discrete particle simulations under highly asymmetric wave conditions. The MP-M model with the analytical stress estimations relatively best predicts the discrete particle simulations. Models based on the quadratic stress law are unable to predict net sediment flux under asymmetric wave condition.

During skewed and combined waves, the spatially and temporally varying mixing provided by Case 3 results in the highest correlation with the discrete particle simulations. However during highly asymmetric waves, the uniform mixing provided

by the Case 1 enhances the mixing near the bed and during the period of flow reversal when accelerations are largest, which results in the highest correlation with the discrete particle simulations. This result supports the hypothesis that alternative mixing mechanisms may be present at the fluid-sediment interface under waves with large accelerations.

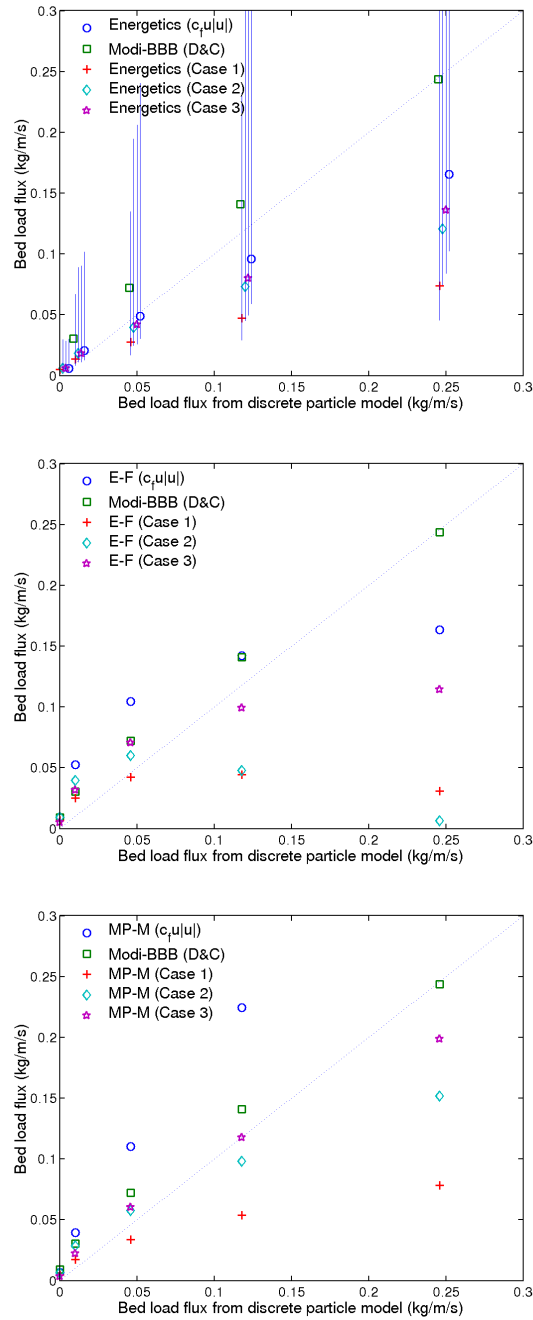


Figure 4.7: Comparisons of predicted time-averaged sediment flux by energetics based (top panel), E-F (middle panel), and MP-M (bottom panel) bed load sediment transport models with those simulated with the discrete particle model (Drake and Calantoni, 2001) under the skewed wave condition ( $\phi = 0$ ). The errorbars show the flux range with  $\epsilon_b = 0.13 - 1.03$ .

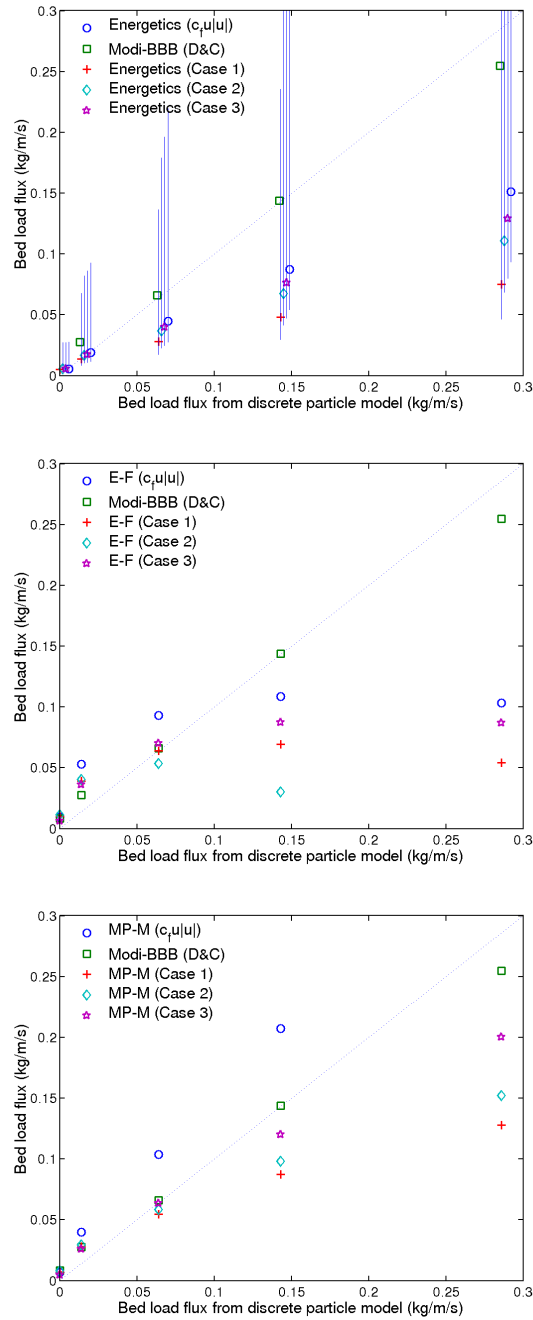


Figure 4.8: Comparisons of the predicted time-averaged sediment flux by energetics based (top panel), E-F (middle panel), MP-M (bottom panel) bed load sediment transport models with those simulated with the discrete particle model (Drake and Calantoni, 2001) under the combined wave condition ( $\phi = \pi/4$ ). The errorbars show the flux range with  $\epsilon_b = 0.13 - 1.03$ .

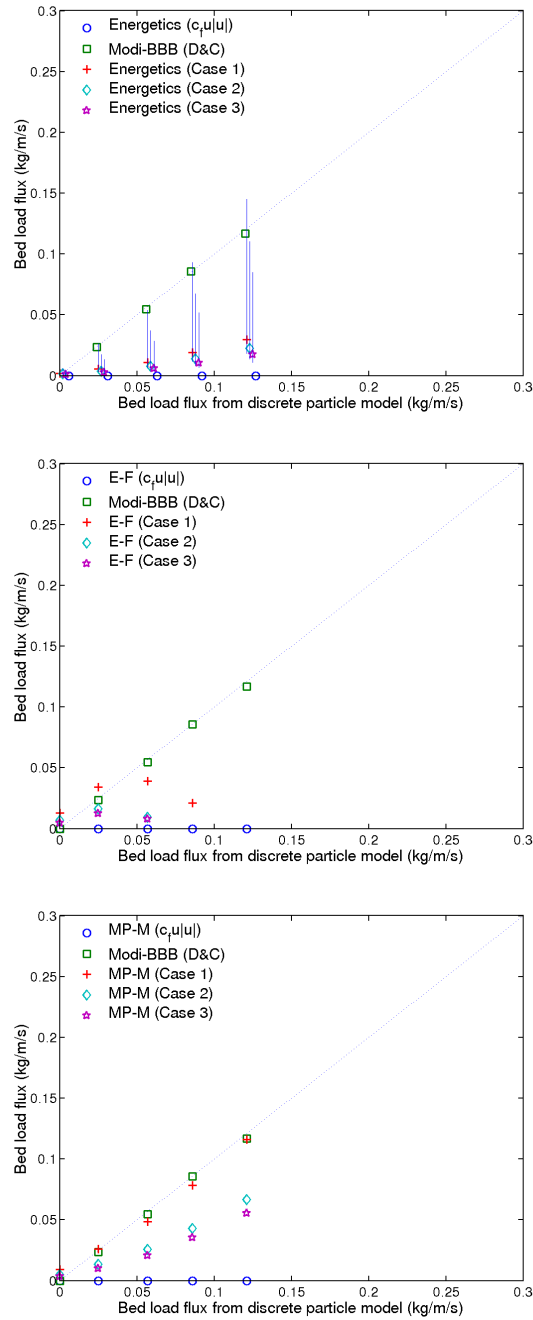


Figure 4.9: Comparisons of the predicted time-averaged sediment flux by energetics based (top panel), E-F(middle panel), and MP-M (bottom panel) bed load sediment transport models with those simulated with the discrete particle model (Drake and Calantoni, 2001) under the asymmetric wave condition ( $\phi = \pi/2$ ). The errorbars show the flux range with  $\epsilon_b = 0.13 - 1.03$ .

## CHAPTER 5

### CONCLUSIONS

Solutions to the quasi-steady wave bottom boundary layer equation have been derived for three different eddy viscosity formulations. The eddy viscosity formulations include: constant eddy viscosity (Case 1), spatially varying eddy viscosity (Case 2), and temporally and spatially varying eddy viscosity (Case 3).

The three bottom boundary layer models are calibrated and evaluated with laboratory observations by Jonsson and Carlsen (1976) and Jensen *et al.* (1989), and field observations from Duck94. The spatially varying eddy viscosity models (Case 2 and Case 3) better predict the horizontal velocity and bed stress amplitudes. The temporally and spatially varying eddy viscosity model (Case 3) best predicts the phase of bed stress.

Predictions of bed stress from the three analytical boundary layer models and a quadratic stress law are used for the stress formulations in three separate bed load sediment flux models. The bed load flux models include a beach-scale energetics based model and the boundary-layer-scale models of Meyer-Peter and Müller (1948) and Engelund and Fredsøe (1976). The three bed load models are evaluated with the granular-scale discrete particle simulations of Drake and Calantoni (2001).

The time-varying bed load sediment flux comparisons reveal that almost all net sediment flux under non-linear wave-dominated conditions are in the onshore direction, this results is consistent with the results from the discrete particle simulations of Drake and Calantoni (2001). The predicted time-varying bed flux amplitudes are generally comparable to the discrete particle simulations. The energetics based model predicts time-varying sediment flux amplitude that is 10% lower than the E-F and MP-M models. The constant eddy viscosity model (Case 1) predicts a lower amplitude than the spatially varying eddy viscosity models (Case 2 and Case 3) in both onshore and offshore directions for both purely skewed and combined waveforms. However, the constant eddy viscosity model (Case 1) predicts comparable amplitude to the other models for the purely asymmetric waveform.

The time-averaged bed load sediment flux comparisons show that the energetics based bed load sediment transport model and the MP-M model predict increasing time-averaged sediment flux when wave amplitude increases, while the predictions of the E-F model predict peak fluxes when the wave amplitude exceeds 1.0 m/s. The bed load models with analytical bed stress estimations predict lower time-averaged bed load fluxes than the discrete particle simulations of Drake and Calantoni (2001). Energetics based models can predict 20% – 60% of the time-averaged flux of the discrete particle simulations when the bed load efficiency is 0.21. As the sediment flux in the energetics based model is a linear function of the bed load efficiency, the model skill can be improved by increasing this value. However, an increase in the bed load efficiency cannot resolve the time-averaged flux amplitude for the purely asymmetric wave condition. The MP-M model with the analytical bed stress estimations shows the best model performance with amplitudes ranging from 30% – 90% of the discrete

particle simulation amplitudes. In general, the spatially varying eddy viscosity formulations (Case 2 and Case 3) included in the MP-M model outperform the constant eddy viscosity model (Case 1). The exception to this is the purely asymmetric wave case when the spatially varying formulations predict significantly lower fluxes when compared to the constant eddy viscosity model (Case 1). This result may indicate additional transport generation mechanisms during the purely asymmetric wave case when fluid accelerations are high.

## APPENDIX A

### DATA ANALYSIS IN DUCK94 FIELD EXPERIMENT

For the field observations in the Duck94 field experiment on the Outer Banks of the North Carolina coast, the bed shear stress is estimated based on the bottom boundary layer velocity profile, following Foster *et al.* (2000),

$$\tau_b = \kappa z_o u_* \left. \frac{\partial u}{\partial z} \right|_{z=z_o} \quad (\text{A.1})$$

where,  $\tau_b$  is the bed shear stress,  $\kappa = 0.41$  is the Von Karman's constant,  $z_o$  is the bed level,  $u_*$  is the bed shear velocity, which is estimated with the formulation

$$u_* = \kappa z_o \left. \frac{\partial u}{\partial z} \right|_{z=z_o} \quad (\text{A.2})$$

The velocity gradient at the bed is approximated with the rms horizontal velocity observations

$$\left. \frac{\partial u}{\partial z} \right|_{z=z_o} \approx \sqrt{2} \left[ \alpha u_{rms}(z_o) + \beta u_{rms}(z_o + \Delta z_1) + \gamma u_{rms}(z_o + \Delta z_2) \right] \quad (\text{A.3})$$

The coefficients are determined by Foster (1996), as

$$\begin{aligned} \alpha &= \frac{-z_1^2 + z_2^2}{z_1 z_2 (z_1 - z_2)} \\ \beta &= \frac{-z_2}{z_1 (z_1 - z_2)} \\ \gamma &= \frac{z_1}{z_2 (z_1 - z_2)} \end{aligned} \quad (\text{A.4})$$

Assuming the velocity at  $z_o$  is zero, the velocity gradient is approximated with

$$\left. \frac{\partial u}{\partial z} \right|_{z=z_o} \approx \sqrt{2} \left( -\frac{\Delta z_2}{\Delta z_1(\Delta z_1 - \Delta z_2)} u_{rms}(z_o + \Delta z_1) + \frac{\Delta z_1}{\Delta z_2(\Delta z_1 - \Delta z_2)} u_{rms}(z_o + \Delta z_2) \right) \quad (\text{A.5})$$

## APPENDIX B

### SOLUTION CONVERGENCES OF THE BOTTOM BOUNDARY LAYER MODELS

In this chapter, the discussion focuses on the solution convergences of the bottom boundary layer models, especially the model's sensitivity to the upper boundary,  $d$ , and mode number of the eigenvalues,  $N$ .

The sensitivity of the constant eddy viscosity boundary layer model (Case 1) to the upper boundary elevation,  $d$ , is examined with the rms deviation of the model velocity solution between a domain size of 50 cm and domain sizes of 10, 20, 30, and 40cm (left panel of Figure B.1). As shown in the figure, the results at lower elevation are very sensitive to the upper boundary. In the simulations, the upper boundary was chosen as  $d = 30\text{cm}$ . The normalized rms deviation between upper boundary sizes of 30 and 50 cm has a maximum of 20% at the bed.

Series convergence is assumed when the rms of a given mode amplitude ( $a_{n_{rms}}$ ) is  $< 1\%$  of the summed rms of the previous mode amplitude. For the constant eddy viscosity model, 50 modes were chosen in the simulations (right panel of Figure B.1).

Figure B.2 shows the spatially varying eddy viscosity boundary layer model's (Case 2) sensitivity to the upper boundary elevation,  $d$ . Like Case 1, the results at lower elevation are relatively sensitive to the upper boundary, but the influence is not

as significant as in Case 1. In the simulations, the upper boundary was also chosen as  $d = 30\text{cm}$ . The normalized rms deviation between upper boundary sizes of 30 and 50 cm has a maximum of 0.06% at the bed.

Similar to Case 1, series convergence is also assumed when the rms of a given mode amplitude ( $a_{n_{rms}}$ ) is  $< 1\%$  of the summed rms of the previous mode amplitude. For the spatially varying eddy viscosity model, only 15 modes were chosen in the simulations (right panel of Figure B.2).

Figure B.3 shows the temporally and spatially varying eddy viscosity boundary layer model's (Case 3) sensitivity to the upper boundary elevation,  $d$ . Like Case 2, the results at lower elevation are relatively sensitive to the upper boundary, but the influence is similar to Case 2 and less significant than in Case 1. In the simulations, the upper boundary was also chosen as  $d = 30\text{cm}$ . The normalized rms deviation between upper boundary sizes of 30 and 50 cm has a maximum of 0.06% at the bed.

Similar to Case 1 and 2, series convergence is also assumed when the rms of a given mode amplitude ( $a_{n_{rms}}$ ) is  $< 1\%$  of the summed rms of the previous mode amplitude. For the temporally and spatially varying eddy viscosity model, 15 modes were chosen in the simulations (right panel of Figure B.2).

Totally, the constant eddy viscosity model (Case 1) is more sensitive to the upper boundary layer elevation than the spatially varying eddy viscosity models (Case 2 and 3). The upper elevations were all chosen as  $d = 30\text{cm}$ . The largest normalized rms deviation exists in Case 1. More modes of eigen values were used in Case 1 (50) than Case 2 and 3 (15).

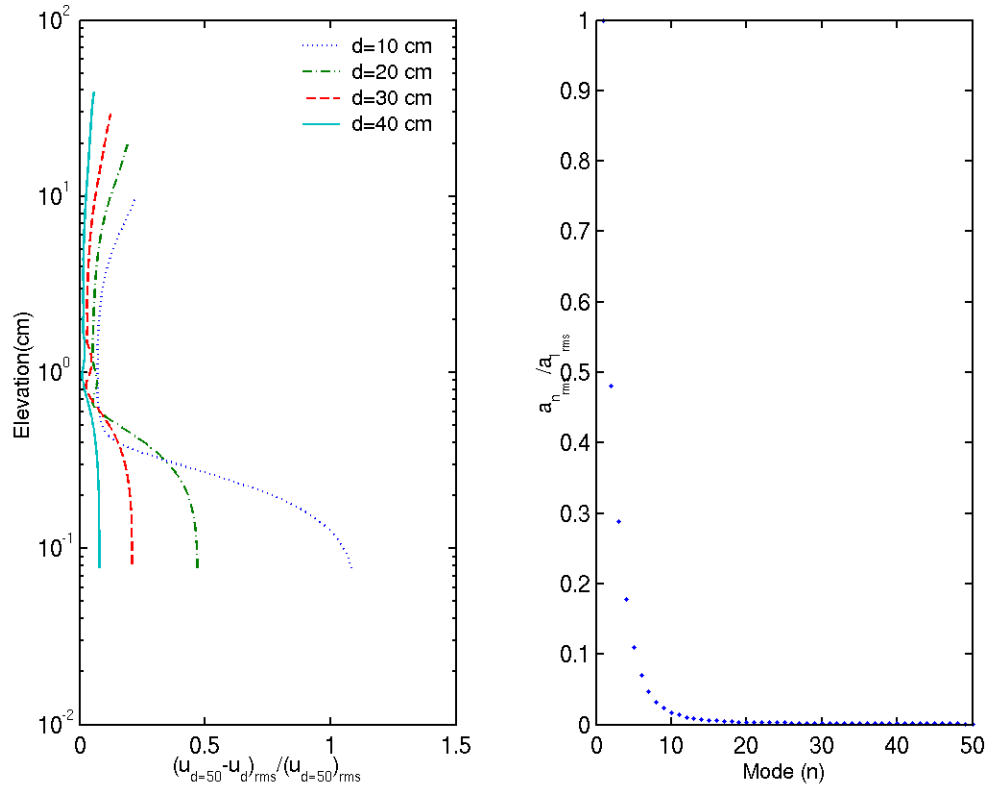


Figure B.1: The rms deviation between velocity results from the constant eddy viscosity model (Case 1) with a 50 cm upper boundary and with 10, 20, 30, and 40 cm upper boundaries normalized by the rms of the velocity results with a 50 cm upper boundary (left panel); the rms of the amplitude normalized by the rms of the first mode amplitude.

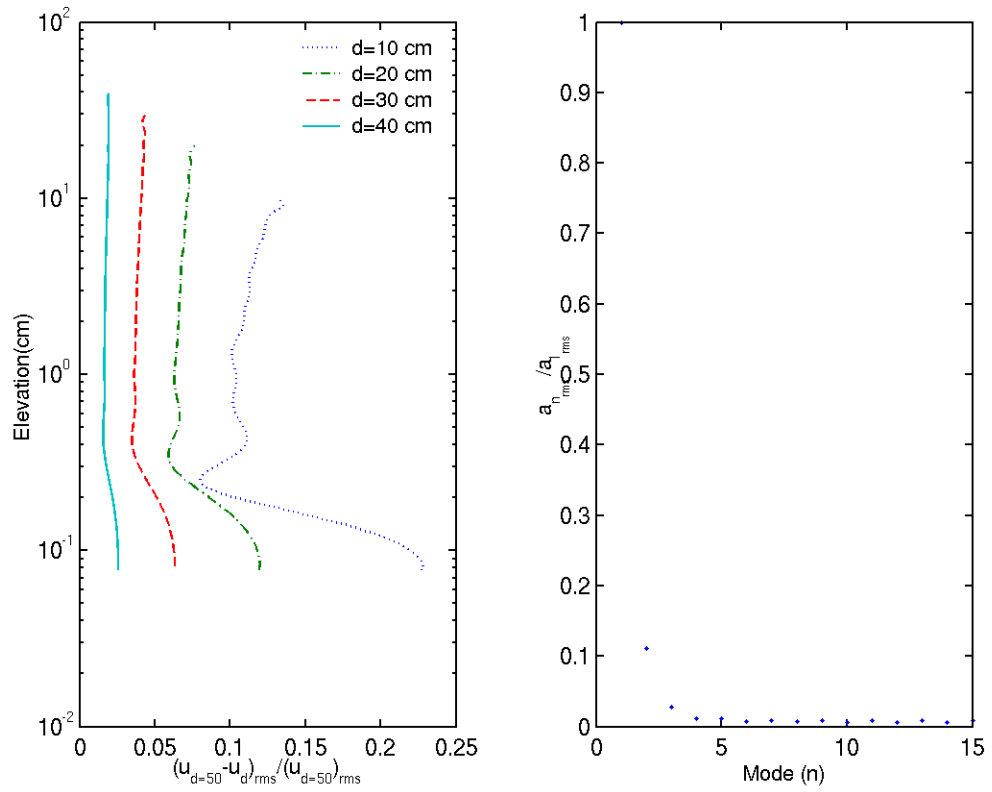


Figure B.2: The rms deviation between velocity results from the spatially varying eddy viscosity model (Case 2) with a 50 cm upper boundary and with 10, 20, 30, and 40 cm upper boundaries normalized by the rms of the velocity results with a 50 cm upper boundary (left panel); the rms of the amplitude normalized by the rms of the first mode amplitude.

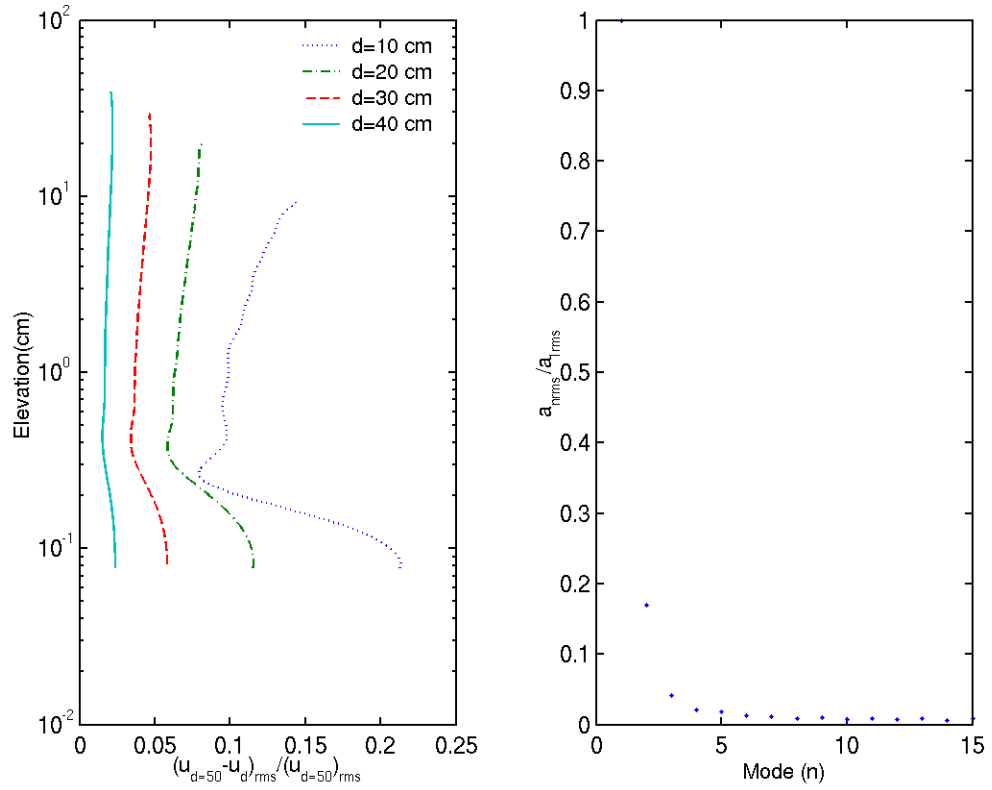


Figure B.3: The rms deviation between velocity results from the temporally and spatially varying eddy viscosity model (Case 3) with a 50 cm upper boundary and with 10, 20, 30, and 40 cm upper boundaries normalized by the rms of the velocity results with a 50 cm upper boundary (left panel); the rms of the amplitude normalized by the rms of the first mode amplitude.

## BIBLIOGRAPHY

- Bagnold, R. A. (1966). An approach to the sediment transport problem from general physics. *U.S. Geol. Surv. Prof. Pap.*, 422(1):1–37.
- Bailard, J. A. (1981). An energetics total load sediment transport model for a plane sloping beach. *J. Geophys. Res.*, 86(C11):938–954.
- Bowen, A. J. (1980). Simple models of nearshore sedimentation; beach profiles and longshore bars. in *The Coastline of Canada*, edited by S.B. McCan, *Pap. Geol. Surv. Can.*, 80-10:1–11.
- Dalrymple, R. A. (2001). Shoring up coastal engineering. *Civil Engineering*.
- Drake, T. G. and Calantoni, J. (2001). Discrete particle model for sheet flow sediment transport in the nearshore. *J. Geophys. Res.*, 106(C9):19859–19868.
- Einstein, A. (1906). *Ann. Phys, Lpz*, 20:627–633.
- Elgar, S., Gallagher, E. L., and Guza, R. T. (2001). Nearshore sandbar migration. *J. Geophys. Res.*, 106(C6):11623–11627.
- Engelund, F. A. and Fredsøe, J. (1976). A sediment transport model for straight alluvial channels. *Nordic Hydrology*, 7(5):293–306.
- Foster, D. L. (1996). *Dynamics of the Nearshore Wave Bottom Boundary Layer*. PhD thesis, Oregon State University.
- Foster, D. L., Beach, R. A., and Holman, R. A. (2000). Field observation of the wave bottom boundary layer. *J. Geophys. Res.*, 105(C8):19631–19647.
- Foster, D. L., Guenther, R. A., and Holman, R. A. (1999). An analytic solution to the wave bottom boundary layer governing equation under arbitrary wave forcing. *Ocean Eng.*, 26:595–623.
- Fredsøe, J. and Deigaard, R. (1992). *Mechanics of Coastal Sediment Transport*. World Scientific.
- Gallagher, E. L., Elgar, E., and Guza, R. T. (1998). Observations of sandbar evolution on a natural beach. *J. Geophys. Res.*, 103(C2):3203–3215.
- Hoefel, F. and Elgar, S. (2003). Wave-induced sediment transport and sandbar migration. *Science*, 299:1885–1887.

- Hsu, T.-J., Elgar, S., and Guza, R. T. (2004). A wave-resolving approach to modeling onshore sandbar migration. *J. Geophys. Res.* (*accepted*).
- Hsu, T.-J. and Hanes, D. M. (2004). Effects of wave shape on sheet flow sediment transport. *J. Geophys. Res.*, 109(C05025):doi:10.1029/2003JC002075.
- Jensen, B. L., Sumer, B., and Fredsøe, J. (1989). Turbulent oscillatory boundary layers at high reynolds numbers. *J. Fluid Mech.*, 206:265–297.
- Jonsson, I. G. and Carlsen, N. A. (1976). Experimental and theoretical investigations in an oscillatory turbulent boundary layer. *Journal of Hydraulic Research*, 14:45–60.
- Meyer-Peter, E. and Müller, R. (1948). Formulas of bed-load transport. In *Rep. 2nd Meet. Int. Assoc. Hydraul. Struct. Res.*, pages 39–64, Stockholm.
- Nielsen, P. (1992). *Coastal bottom boundary layers and sediment transport*. World Scientific.
- Nikuradse, J. (1933). Stromungsgesetze in glatten und rauhen rohren. *V D I Forschungsheft, Berlin*, 361.
- Sleath, J. F. A. (1999). Conditions for plug formation in oscillatory flow. *Continental Shelf Research*, 19:1643–1664.
- Thornton, E. B., Humiston, R. T., and Birkemeier, W. (1996). Bar/trough generation on a natural beach. *J. Geophys. Res.*, 101(C5):12097–12110.